

THE ORBIT OF CHARON IS CIRCULAR

MARC W. BUIE¹, DAVID J. THOLEN², AND WILLIAM M. GRUNDY³

¹ Southwest Research Institute, 1050 Walnut Street, Suite 300, Boulder, CO 80302, USA; buie@boulder.swri.edu
² Institute for Astronomy, University of Hawaii, 2680 Woodlawn Drive, Honolulu, HI 96822, USA; tholen@ifa.hawaii.edu
³ Lowell Observatory, 1400 W. Mars Hill Road, Flagstaff, AZ 86001, USA; w.grundy@lowell.edu

Received 2012 March 14; accepted 2012 May 1; published 2012 June 7

ABSTRACT

We present a detailed analysis of the orbit of Charon where we show its orbit to be circular. This analysis explores the effects of surface albedo variations on the astrometry and the resulting errors in the orbital elements. We present two new epochs of data from the *Hubble Space Telescope* taken in 2008 and 2010 and combine that with a re-analysis of previously published data from 1992 and 2002. Our adopted two-body Keplerian orbital elements for Charon are $P = 6.3872273 \pm 0.0000003$ days, $a = 19573 \pm 2$ km, $e = 0.$, $i = 96.218 \pm 0.008$ deg, $L = 4.50177 \pm 0.00018$ rad, and $\Omega = 3.89249 \pm 0.00012$ rad for an epoch of JDT = 2452600.5 in the J2000 reference frame. The 1σ upper limit to the eccentricity is 7.5×10^{-5} . The predicted uncertainty in the position of Charon relative to Pluto at the time of the New Horizons encounter based on this orbit is 8 km.

Key words: astrometry – ephemerides – planets and satellites: individual (Pluto, Charon)

Online-only material: color figures, Supplemental data (FITS) file (tar.gz)

1. INTRODUCTION

Orbit determination for Charon might reasonably be expected to be a solved problem by now. Although astrometry for Charon spans more than three decades, there are still questions regarding the absolute scale of the system and the orbital eccentricity. The best astrometry so far comes from the *Hubble Space Telescope* (*HST*), and that data set alone now spans nearly 20 years.

All measurements of Pluto system objects are currently made with respect to some reference point within the system. For computational convenience, this reference point is usually chosen to be Pluto since it is always directly observable and is the most massive object in the system. However, the measured position must be of its mass center (assumed to be the same as body center) for it to lead to a successful orbit determination.

Prior work of Tholen & Buie (1997) and Buie et al. (2010b) has already established the magnitude and importance of the Pluto surface albedo distribution on its measured position. Unfortunately, as most observations do not resolve the body of Pluto, they get a position by measuring a photo-center. The difference between the center of light (COL) and the center of body (COB), referred to here as COL–COB, introduces systematic errors in the astrometry if not fully corrected. Attempts were made to correct for COL–COB in that previous work, but it is difficult to ascertain the accuracy of these corrections. The fact that Pluto is tidally locked with Charon’s orbit makes it even harder to disentangle since the photo-center modulation is precisely synchronous with orbital motion.

This paper provides an in-depth look at what a surface albedo distribution on Pluto can do to the inferred orbital properties of Charon. We explore simplified ideal cases and investigate the consequences of the currently published albedo maps. We also present new astrometric observations with *HST*. All of our large *HST* data sets are then analyzed and new two-body Keplerian orbit fits are presented along with corrections for systematic errors that, until now, have confused the orbit determination.

2. COMPUTATIONAL METHODOLOGY

The state of the art in fitting orbital motion within the Pluto system requires a fully perturbed N -body-integrated solution (Lee & Peale 2006; Tholen et al. 2008). However, Charon’s orbit is very nearly equal to simple two-body Keplerian motion. For the purposes of this work we restrict ourselves to the two-body problem. We begin this analysis by considering a contrived problem chosen to mimic the Charon data set but with orbital elements and Pluto surface properties that we construct and thus know and control.

The first step is to adopt orbital elements for our tests. We chose two main sets, one of which is very similar to currently published orbits for Charon. In particular, we wanted to test our sensitivity to orbital eccentricity. Thus, one set has a nominal eccentricity similar to previous values, while the other is perfectly circular. For each set of elements we compute perfect astrometric values for a set of chosen observation times. In all cases we assume that the heliocentric orbit of the Pluto system barycenter is perfectly known and use it to incorporate the proper viewing geometry. These perfect values form the basis for our calculation. In these calculations and the fitting to follow we use the JPL DE421 ephemeris for the heliocentric orbit of Pluto. The chosen elements for Charon are thus used to compute perfectly known differential astrometry for each time. The temporal sample was chosen to represent key epochs in prior Pluto observations (1985, 1991, 2002, and 2011). Each year contains 12 points evenly spaced over a single rotation. We also did a test using the actual data sample times from the real astrometric data.

Given a set of perfect astrometry, we can fit for the orbital elements. This step serves as a test that our fitting program can accurately return the known orbit. Note that this process naturally incorporates the finite time span of the data into the fit. This fit to the perfect astrometry is one reference against which we compare other solutions. We also use the original orbit as a reference. Usually these two references are the same. In cases where there is a non-zero eccentricity, the fitting program

does indeed return the original orbital elements. The situation is different when the original orbit has $e = 0$. In this case, the fitting program returns a non-zero but small eccentricity for the perfect data and provides a useful comparison for cases where we attempt to fit eccentricity when the orbit happens to be circular.

The next layer to our analysis comes from adding noise to the perfect astrometry. The amount of noise is controlled and is normally distributed with a fixed size for all observations. Fitting these noisy values is a useful baseline to show how well we can reconstruct the orbit with just the complications from random measurement noise.

The final element of our test comes from adding a COL–COB offset to the synthetic data. These tests show whether the retrieved orbital elements are still consistent with the known orbit. We can use this method to test different maps that can be either entirely fake constructs or a map that is believed to relate to the surface of Pluto.

The fitting process uses the same orbit fitting tools as Grundy et al. (2007) but modified to fit for $e \cos \omega$ and $e \sin \omega$ instead of e and ω (though we still report the latter). We start from an initial guess that is modified slightly from the known elements. The data are then fitted using a nonlinear least-squares minimization “amoeba” routine (Press et al. 1992). The convergence criteria were set to a change in chi-square of 2×10^{-7} . For a given set of data, this fitter is used up to 300 times. Each fitting attempt runs until the amoeba fitter quits with a claim of convergence. If the fitted parameters are identical between two successive iterations, the fit is declared complete. If the parameters changed, they are used as the new starting point and the starting scale parameters for building the initial simplex are reset to the starting sizes. Most of the time the fit reaches final convergence in 6–8 iterations. In all cases the fit converged before the retry limit was reached. For each test case, there are 40 trial data sets generated with independent noise each generating its own fitted solution. All fitting results are kept and at the end are averaged for the final parameters. The uncertainty on those parameters is the standard deviation of the values returned from the trials.

We chose test cases based on fake maps and a real map of Pluto. Some of the fake map runs initially used an astrometric noise level of 4 mas (milliarcseconds), but later changed to be 2 mas, a level comparable to the random errors of the *HST* astrometry. For the fake map there are two components introduced, polar caps and equatorial modulation. The size of the polar cap regions was comparable to the size of the missing region in the Buie et al. (2010b) map. The equatorial modulation was set to mimic the Pluto map with a large region that is darker than the average with a brighter extension on the eastern end of the dark spot. The baseline single-scattering albedo was set to $w = 0.8$. The dark spot was set to $w = 0.4$ to get a light-curve amplitude comparable to the Pluto light curve.

The real map tests were based on the *V*-band single-scattering albedo map from Buie et al. (2010b). One extra variable was used to fill in the missing region of the map. We test bright ($w = 0.95$) and dark ($w = 0.05$) end members, as well as an intermediate value ($w = 0.65$) chosen to blend in reasonably well with the constrained portions of the map.

3. SIMULATION RESULTS

The fitting results for the fake data sets based on a non-zero eccentricity are listed in Table 1. Each run is labeled with either a letter code or a number. The TR Run is the adopted “true” set of elements used to compute the perfect astrometry. The RF

Run is the reference from fitting the perfect data. All values in parentheses show the uncertainty of the preceding number in the final digits of the value presented. The horizontal lines separate groups of tests. Runs 0–21 are all based on fake maps, while 22–51 involve the Buie et al. (2010b) map for Pluto. The runs 0–11 were computed with a 4 mas noise level, all others with a 2 mas noise level. The first group (0–2) is based on all four epochs but different fake maps all having the same equatorial modulation: 0, bright north polar cap; 1, no polar cap; and 2, dark north polar cap. The second group (3–16) has no equatorial modulation, only various configurations of polar caps: 4, bright north polar cap; 5, dark south polar cap; 6, bright south polar cap; and 7–16, dark north pole. Runs 17–21 have no polar caps, only equatorial modulation. For runs 22–26 the missing pole on the Buie et al. (2010b) map was set to $w = 0.95$. For runs 27–31 the missing pole was set to $w = 0.05$. The runs 32–46 show the effect of rotating the map by 90° , then 180° , and then 270° relative to the known orientation of Pluto. This rotation also rotates the map relative to the orbit of Charon, causing any map-induced eccentricity to rotate the orbital ellipse in a manner that correlates with the map. The final group from 47–51 uses the nominal Buie et al. (2010b) map with a missing area set to $w = 0.65$ using the actual data sampling times for the *HST* data set.

Table 1 contains a lot of information that can be difficult to absorb. Figures 1–6 depict graphically the results of the synthetic astrometry cases shown in the table. All of the figures have the same basic construction. Along the abscissa is the run number. Each plot shows the indicated orbital element with its uncertainty. The captions for each discuss the implications of the information seen in the individual plots. The vertical lines are drawn in the same locations as the horizontal lines in the table to make it easier to see the groups of runs. The heavy (green) horizontal solid line shows the reference fit (RF). The symbols encode the different data sets used for fitting: the filled (black) circle indicates that all epochs are fit at once, the open (red) pentagon is for 1985 data, the open (magenta) triangle is for 1991 data, the open (blue) square is for 2002 data, and the open (purple) diamond is for 2011 data. Within each subgroup the data sets are arranged in the same chronological order for ease of comparison. Also, the distinction between partial and full data sets is easily seen since only the combined data are filled symbols. The choice of years corresponds to the mutual event season, first epoch of *HST* observations, epoch of *HST* maps of Pluto, and the current epoch.

There are solutions that clearly got the wrong answer, not by many sigma, but enough to be interesting, especially for semimajor axis and eccentricity. In general, tests with all 4 years are the most robust. In particular, the period is insensitive to the albedo map and is always quite close within the noise. Data from a single year often returned elements that were significantly different from the right answer. Also, it seems as if our synthetic 2002 data are particularly prone to getting bad or noisy answers. The most obvious difference is the opening angle of the apparent ellipse, but it is hard to see why that should matter so much. We suspect that changing the synthetic observational cadence by spreading out the observations over a longer baseline or adding extra constraints would change the misfit behavior of the 2002 data. However, we leave this particularly troublesome case in our case study to provide a cautionary example that minimal data sets, such as our synthetic cadence, can lead to a bad determination for the orbit. The last set of cases clearly shows that our actual data sampling cadence does not suffer

Table 1
Two-body Orbit Fits to Simulated Astrometry

Run	P (days)	a (km)	e	i (deg)	Ω (rad)	L (rad)	$\tilde{\omega}$ (rad)
TR	6.387229	19570.2	0.003505	96.169	4.50228	3.89304	0.36328
RF	6.387231(0)	19596(1)	0.0033(00)	96.22(01)	4.5041(1)	3.8943(01)	0.34(0.01)
0	6.387229(2)	19596(18)	0.0073(08)	96.34(06)	4.5031(18)	3.8920(13)	0.58(0.06)
1	6.387229(2)	19593(14)	0.0057(06)	96.35(07)	4.5031(15)	3.8919(12)	0.46(0.08)
2	6.387230(2)	19575(10)	0.0025(06)	96.33(06)	4.5026(17)	3.8920(13)	4.98(2.28)
3	6.387230(2)	19580(13)	0.0023(05)	96.20(06)	4.5032(14)	3.8937(10)	5.16(0.33)
4	6.387230(1)	19609(4)	0.0048(08)	96.23(06)	4.5036(16)	3.8942(12)	0.49(0.08)
5	6.387229(2)	19603(6)	0.0036(06)	96.21(06)	4.5035(14)	3.8940(10)	0.29(0.12)
6	6.387230(2)	19602(6)	0.0034(07)	96.20(06)	4.5032(15)	3.8940(12)	0.60(1.32)
7	6.387264(8)	19615(18)	0.0030(13)	96.19(10)	4.4687(84)	3.8934(19)	3.50(2.51)
8	6.387255(19)	19591(24)	0.0029(10)	96.22(09)	4.486(12)	3.8933(19)	3.84(2.41)
9	6.386(5)	19564(34)	0.0023(06)	96.19(16)	4.54(14)	3.8926(17)	4.76(0.64)
10	6.387343(45)	19570(37)	0.0033(08)	96.16(17)	4.558(20)	3.8937(34)	5.31(0.28)
11	6.387230(2)	19579(11)	0.0022(04)	96.19(06)	4.5027(16)	3.8936(13)	5.00(0.36)
12	6.387262(5)	19615(9)	0.0023(05)	96.20(05)	4.4706(54)	3.8931(09)	4.30(2.31)
13	6.387261(22)	19591(11)	0.0021(05)	96.20(05)	4.482(14)	3.8933(09)	4.77(2.04)
14	6.387(2)	19565(17)	0.0021(04)	96.17(08)	4.517(46)	3.8929(09)	4.77(0.37)
15	6.387342(31)	19570(18)	0.0030(04)	96.17(09)	4.557(15)	3.8935(17)	5.30(0.16)
16	6.387230(1)	19577(6)	0.0022(02)	96.19(04)	4.5027(8)	3.8935(07)	5.01(0.21)
17	6.387264(5)	19599(10)	0.0034(14)	96.11(05)	4.4729(44)	3.8939(10)	4.64(0.30)
18	6.387253(14)	19594(14)	0.0020(07)	96.27(05)	4.492(9)	3.8942(08)	4.95(0.53)
19	6.392(4)	19600(18)	0.0058(09)	96.49(08)	4.38(10)	3.8944(09)	0.50(0.07)
20	6.387407(20)	19632(18)	0.0046(05)	96.54(09)	4.595(11)	3.8977(18)	0.53(0.09)
21	6.387232(1)	19606(3)	0.0040(03)	96.28(03)	4.5054(8)	3.8946(06)	0.43(0.05)
22	6.387260(7)	19598(14)	0.0076(18)	96.17(05)	4.4756(64)	3.8936(09)	4.02(0.06)
23	6.387253(15)	19625(10)	0.0081(14)	96.33(05)	4.492(10)	3.8942(08)	0.71(0.05)
24	6.405(5)	19580(16)	0.0149(10)	96.39(07)	4.04(13)	3.8934(10)	0.62(0.03)
25	6.387411(34)	19620(18)	0.0078(05)	96.41(09)	4.594(16)	3.8967(17)	0.79(0.05)
26	6.387232(1)	19630(4)	0.0077(04)	96.35(04)	4.5055(9)	3.8951(07)	0.73(0.03)
27	6.387269(10)	19600(17)	0.0124(18)	96.22(04)	4.468(10)	3.8940(09)	3.95(0.03)
28	6.387245(27)	19627(12)	0.0094(13)	96.35(05)	4.497(18)	3.8942(09)	0.74(0.04)
29	6.404(6)	19582(18)	0.0148(10)	96.40(07)	4.05(14)	3.8935(10)	0.62(0.03)
30	6.387420(35)	19621(18)	0.0078(05)	96.41(09)	4.599(17)	3.8968(17)	0.79(0.05)
31	6.387233(1)	19630(5)	0.0074(04)	96.36(03)	4.5057(9)	3.8952(07)	0.77(0.03)
32	6.387261(7)	19576(13)	0.0042(15)	96.23(04)	4.472(7)	3.8929(09)	4.20(0.16)
33	6.387265(31)	19581(23)	0.0161(21)	96.28(05)	4.479(21)	3.8909(10)	0.67(0.02)
34	6.391(4)	19537(18)	0.0134(07)	96.29(08)	4.41(10)	3.8877(11)	0.61(0.03)
35	6.387451(42)	19575(16)	0.0078(05)	96.38(09)	4.608(20)	3.8892(18)	0.76(0.05)
36	6.387230(1)	19614(9)	0.0084(05)	96.32(04)	4.5028(8)	3.8920(07)	0.67(0.03)
37	6.387255(7)	19569(15)	0.0101(18)	96.17(05)	4.473(7)	3.8929(08)	3.99(0.04)
38	6.387247(47)	19603(21)	0.0072(19)	96.07(05)	4.487(31)	3.8923(10)	0.71(0.05)
39	6.401(6)	19502(20)	0.0143(11)	95.86(07)	4.13(15)	3.8894(11)	0.62(0.03)
40	6.387510(83)	19520(19)	0.0078(05)	95.93(12)	4.63(4)	3.8898(17)	0.78(0.05)
41	6.387228(1)	19611(10)	0.0072(05)	96.11(04)	4.5017(9)	3.8933(07)	0.74(0.03)
42	6.387255(7)	19646(18)	0.0017(10)	96.15(05)	4.475(7)	3.8932(10)	4.35(1.45)
43	6.387257(47)	19668(22)	0.0168(20)	96.14(05)	4.486(30)	3.8957(10)	0.68(0.02)
44	6.390(3)	19589(18)	0.0135(07)	96.03(08)	4.43(7)	3.8977(11)	0.62(0.03)
45	6.387452(45)	19572(20)	0.0079(05)	95.97(11)	4.613(21)	3.8978(17)	0.77(0.06)
46	6.387231(1)	19633(6)	0.0090(04)	96.15(04)	4.5046(9)	3.8966(07)	0.69(0.02)
47	6.387281(24)	19587(12)	0.0135(08)	96.43(03)	4.483(13)	3.8964(04)	0.74(0.01)
48	6.387208(5)	19618(3)	0.0117(01)	96.47(01)	4.5061(3)	3.8953(02)	0.68(0.01)
49	6.387391(31)	19616(4)	0.0089(01)	96.39(02)	4.546(8)	3.8962(02)	0.76(0.01)
50	6.387450(48)	19627(4)	0.0087(01)	96.41(02)	4.601(21)	3.8968(04)	0.76(0.01)
51	6.387233(1)	19629(3)	0.0096(01)	96.45(01)	4.5074(3)	3.8964(02)	0.72(0.01)

Notes. The Keplerian elements are given in J2000 coordinates at an epoch of JD = 2452600.5.

the problems shown by the idealized 2002 data. In all cases, changing either pole, either up or down, had a minimal effect on the fit though it clearly introduced a mean offset in the differential astrometry.

Rotational modulation clearly does what we expected, and that was to confuse the fit commensurate with the size of the COL-COB shift induced. The Buie et al. (2010b) map affects things more than the artificial map, and that must be

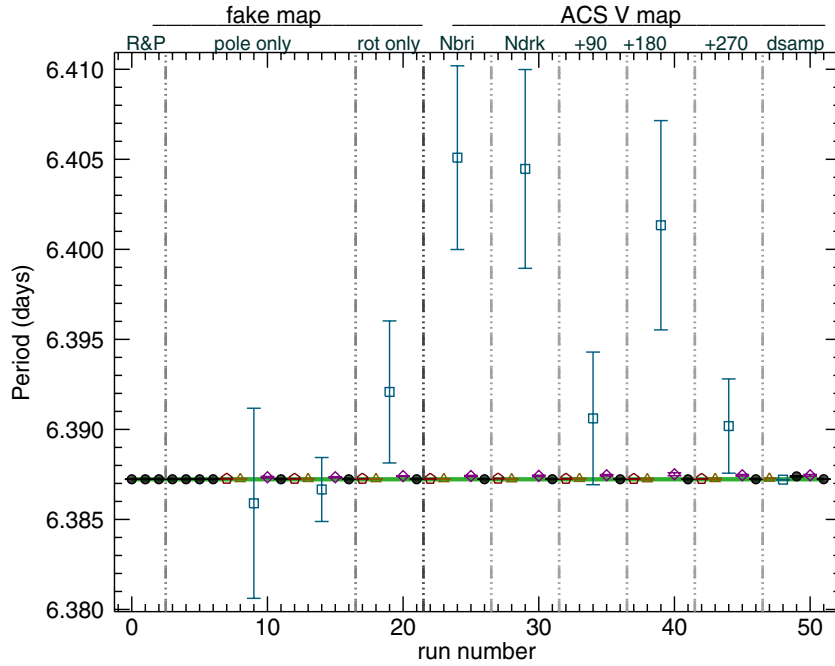


Figure 1. Period: this quantity is faithfully retrieved in most cases to within the uncertainties regardless of the map or data set used. The retrieved errors are quite small and are below the scale of the plot for most points. However, we see the expected correlation between measurement noise, time base of the data, and the uncertainty on the final period. The 2002 data (blue squares) show much higher errors on the retrieved period.

(A color version of this figure is available in the online journal.)

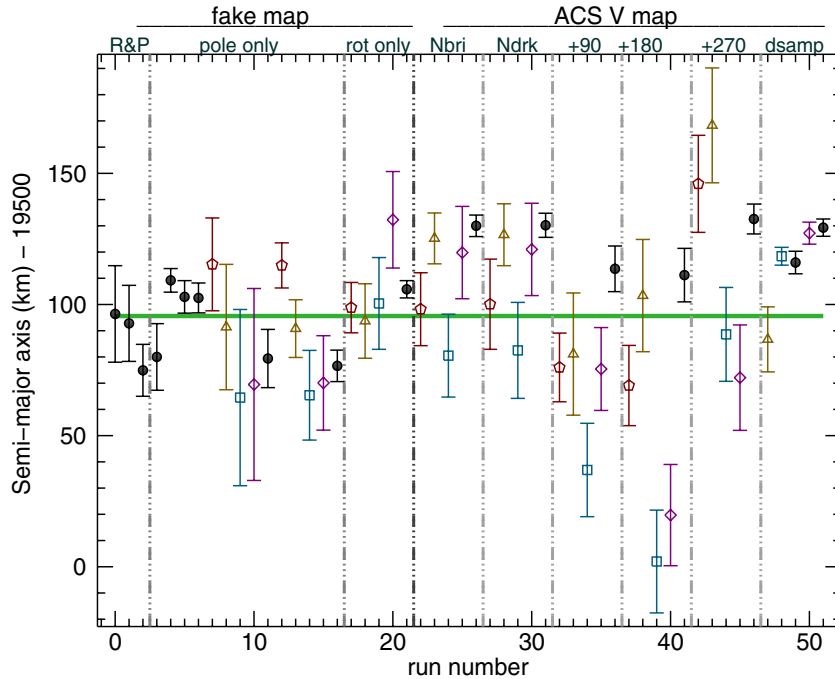


Figure 2. Semimajor axis: the map definitely introduces a systematic error into the determination. The effect is at the 40 km level. Clearly, if one can correct for the map, the error will be reduced. Well-calibrated stellar occultations involving both Pluto and Charon provide a crucial cross-check.

(A color version of this figure is available in the online journal.)

a consequence of being a messier assortment of albedos and not being nicely symmetric. The results from runs 32–46 clearly show that some elements such as i and Ω (not shown) follow the COL–COB effects of the map and not the orbital properties of Charon. Interestingly, we see that the eccentricity is confused by the introduction of the map effects, but the value returned is not obviously connected with the map since the value does

not change with rotating the map. This last point is a crucial revelation with regard to the analysis of the *HST* astrometry in the next section.

Sliding the map in longitude for the Buie et al. (2010b) map clearly changes the nature and placement of the misfit of some elements. There is clearly a correlation between a , e , i , and Ω that depends on the phasing of the map and the orbit for Charon.

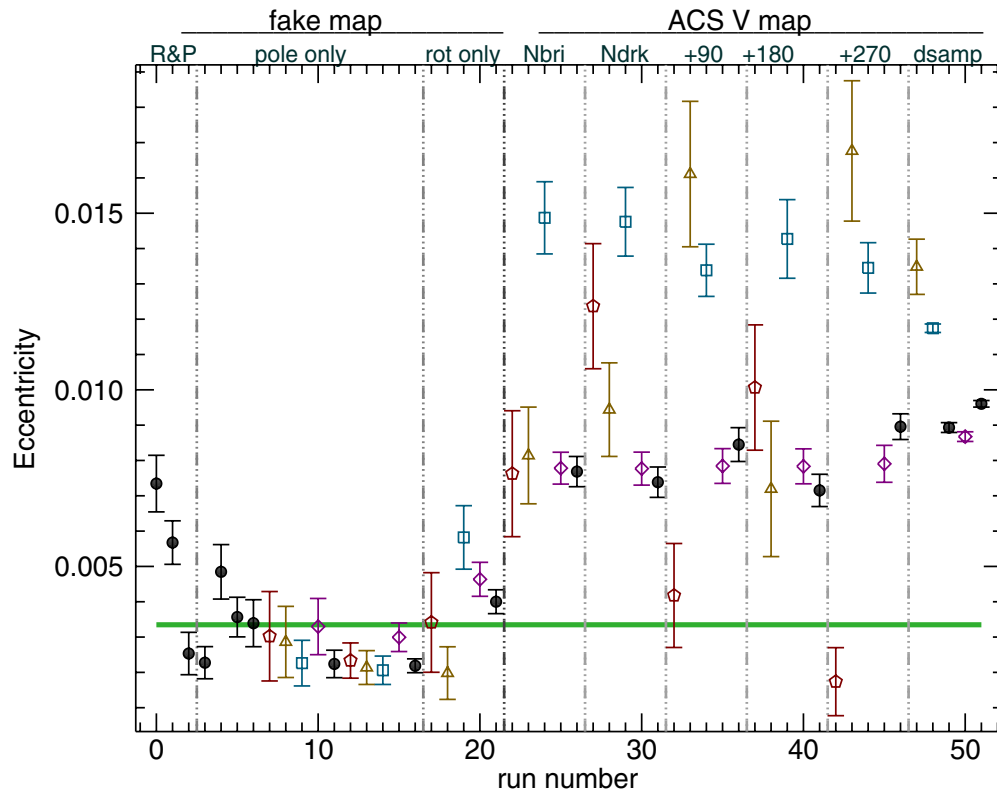


Figure 3. Eccentricity: this orbital element was poorly retrieved. The answer for the final fit depends on the data, on the map, and on every assumption. We can certainly rule out large eccentricities, and these tests suggest a credible upper limit of around 0.01 when no map corrections are applied. (A color version of this figure is available in the online journal.)

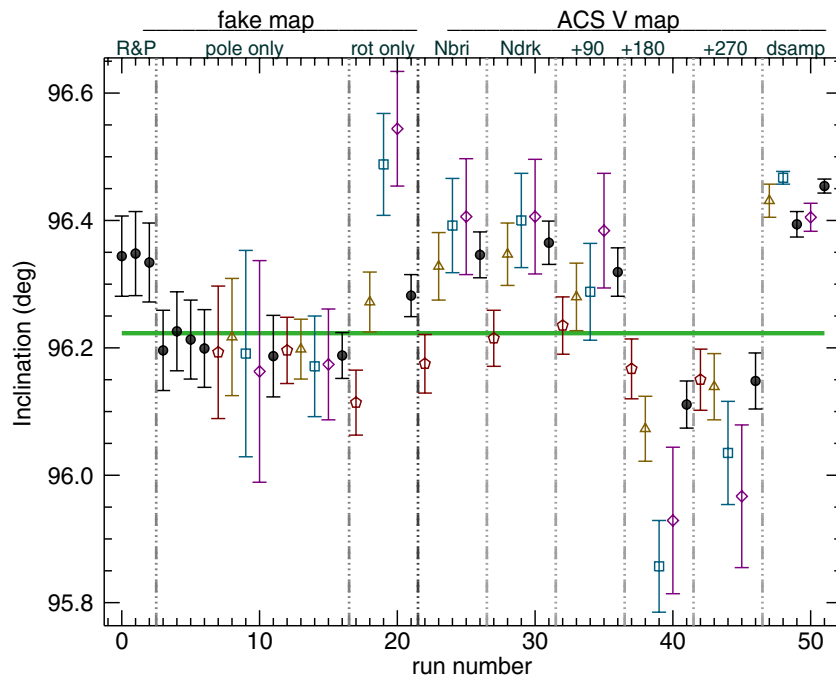


Figure 4. Inclination: there are significant trends here. The answer really does drift with time, and the combined solution hits the mean of that and shows a systematic error. The behavior of Ω is nearly identical to the inclination. (A color version of this figure is available in the online journal.)

4. CHARON OBSERVATIONS

The complete astrometric record for Charon consists of data from photographic plates, speckle interferometry, *HST* imaging,

ground-based adaptive optics (AO) imaging, and most recently occultations involving Pluto and Charon against the same star. We do not attempt to analyze all of these data sets here but instead work with the largest and most homogeneous data from

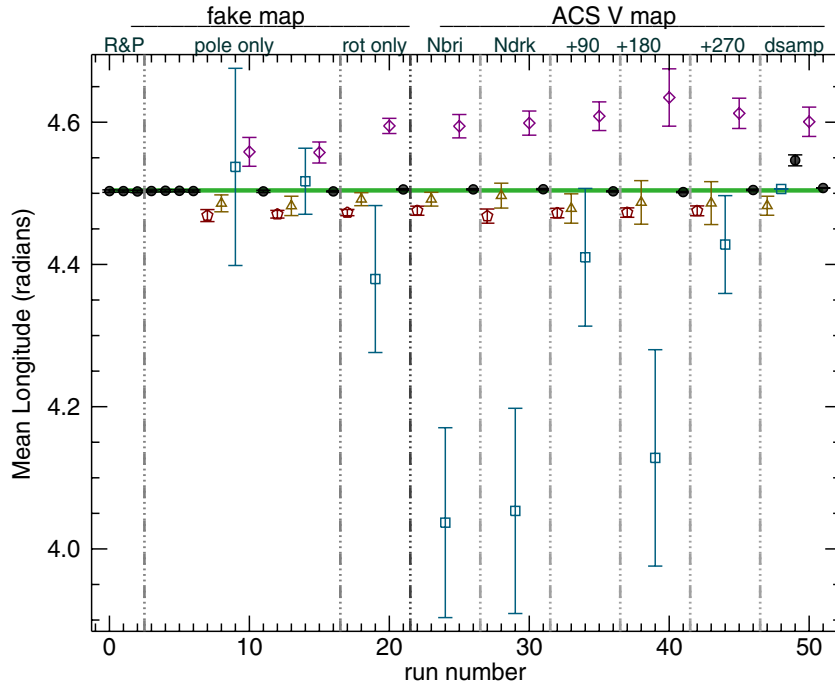


Figure 5. Mean longitude (at the epoch) (L): there are significant trends here. As expected, L is more poorly determined in our tests with shorter time-base data. When combining all epochs, this element is quite well determined and not affected by the COL–COB complication. Once again, the 2002 epoch is particularly problematic. (A color version of this figure is available in the online journal.)

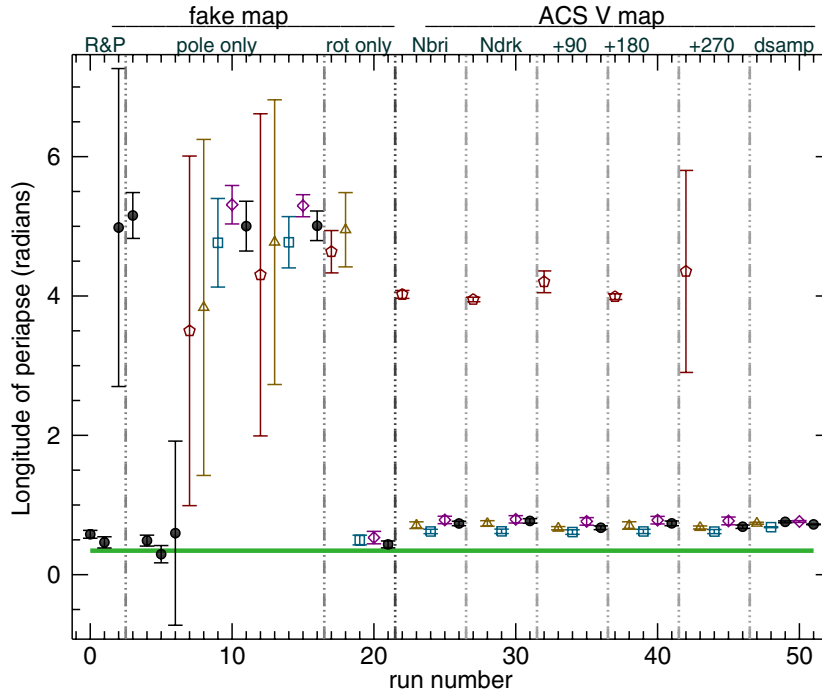


Figure 6. Longitude of periape ($\tilde{\omega}$): the difficulty of retrieving this element is coupled to the problem of determining the eccentricity. If the COL shifts induce a fake eccentricity, then it seems reasonable that the longitude of periape can also be strongly perturbed. In this case, the problems are larger for the synthetic maps, though that is something of a surprise. More interesting is the different behavior of misfit for the 1985 epoch data, where the retrieved value is nearly 180° away from the correct answer. The other epochs with the Buie et al. (2010b) map, including all epochs, get a consistently wrong answer. Thus, even if $\tilde{\omega}$ shows a consistent value with different data sets, it cannot be used to infer whether a correct value has been determined.

(A color version of this figure is available in the online journal.)

HST. Also, understanding the systematic errors requires a reasonably dense data set. For this reason, we restrict this analysis to just those data sets we have collected on *HST*. These data include two epochs of previously published data from Cycle 2

and Cycle 11, as well as two new epochs of data from Cycle 15 and Cycle 17.

With the discovery of additional satellites beyond Charon, the real frontier in orbit determination requires a fully perturbed

N-body solution. However, the masses of the exterior satellites are low enough that any perturbations on Charon are quite small such that a two-body Keplerian orbit is still an excellent approximation. In this work we will restrict our fits to two-body orbits on just Charon.

All of the fitting for this work assumes a geocentric viewpoint and thus does not include the actual location of *HST* during the observations. This correction was included in our Cycle 2 work but is negligible when compared to the other measurement errors. The location of the Pluto–Charon barycenter is computed from the JPL DE421 ephemeris. The use of a different ephemeris will change the viewing direction slightly more than the geocentric approximation but induces changes smaller than the uncertainties. In this section we discuss the old data and present the new data and then move on to fitting orbits.

4.1. *HST* Cycle 2: WFPC/PC, 1992–1993

These data were published in Tholen & Buie (1997) and were the first to show what appeared to be a statistically significant non-zero eccentricity for Charon’s orbit. These observations are of the COL of both bodies. Most of the data were taken with an F555W (V) filter, while a much smaller set used an F435W (B) filter. There are 60 measurements in all covering the time range from 1992 May 1 to 1993 August 18. No uncertainties were measured directly for this work, but the adopted uncertainty is 2.4 mas for most data. These observations also featured a special effort to calibrate the plate scale of the WFPC/PC camera using the heliocentric motion of the Pluto system. These data were taken prior to the deployment of corrective optics, and the spatial resolution was insufficient to provide disk-resolved information on Pluto.

4.2. *HST* Cycle 11: ACS/HRC, 2002–2003

These data were discussed at length in Buie et al. (2006), Tholen et al. (2008), Buie et al. (2010a), and Buie et al. (2010b) but were never tabulated. This data set is unique in this work because we were able to directly measure the COB simultaneously with an albedo map. There are a total of 384 measurements, half taken with the F435W filter and half with the F555W filter, all with the Advanced Camera for Surveys (ACS)/HRC instrument. As with the Cycle 2 data, the uncertainties are estimated by the level of scatter in the observations and was set to 2 mas.

4.3. *HST* Cycle 15: WFPC2/PC, 2007

These observations were supposed to be a repeat of the Cycle 11 data set with the ACS/HRC camera but further optimized to also get better measurements of Nix and Hydra. Unfortunately, the camera failed shortly before observations were scheduled to begin. The WFPC2/PC camera was used in the replanned observations. The pixel scale of this camera is coarse enough that disk-resolved information on Pluto is not possible.

There were a total of 215 images taken with filters F439W, F555W, F606W, F675W, and F814W. The observation pattern included short, medium, and long exposures. In these Pluto is at 80% of full well in the short exposures, Charon is at 80% of full well in the medium exposures while Pluto is slightly saturated, and both Pluto and Charon are badly saturated in the long exposures optimized for measuring Nix and Hydra.

Each image was fitted for the positions and fluxes of Pluto and Charon. The fit consists of an amoeba least-squares minimization of a model image. The model image is constructed using

version 6.2 of TinyTim (Krist 2004) at nominal focus. The normalized model point-spread function (PSF) is computed with $3\times$ oversampling so that the result can be interpolated accurately. Scaling the PSF for the object flux requires a simple multiplicative factor. Placing the PSF in the right location is considerably more involved. To minimize the amount of computations needed for the fitting, a library of PSFs is maintained on a 50 pixel grid in the WFPC2/PC focal plane. When a model image is needed at a particular location, the nearest grid point is used to provide the PSF. The size of the grid is a compromise between smaller changes between grid points and computation speed. When a model PSF is computed, we use sinc interpolation to find the sub-pixel location of the peak of the PSF image and save this information with the PSF in the library.

When a synthetic object is to be placed in a model image, the relevant PSF is loaded along with its peak location. A shift amount is computed from the desired location to the PSF location so that when the PSF is shifted and downsampled to the observing image pixel grid, the peak position is placed where the desired object location is. This extra complexity is necessary to get accurate positions with an undersampled detector since a traditional centroid does not fully account for the undersampling and it will tend to be granularized. This shifted and downsampled PSF is then scaled by the desired flux and added to the model image. The variation of PSF with source color is very weak so all calculations used the color code 12 in TinyTim (slightly redder than the Sun) to most closely match the color of all objects in the system.

Fitting for Pluto and Charon requires that the positions and fluxes be solved simultaneously since their PSFs overlap. One additional step is added for the Pluto image since it is almost resolved. Pluto is additionally convolved with a top-hat filter intended to match the size of its apparent disk. This simulates a uniform disk and serves to blur out the Pluto PSF by a slight amount. At the end there is one more blurring step that is labeled as “jitter” in our software. It was introduced to simulate telescope tracking and pointing jitter and is computed as a Gaussian convolution kernel with a $1/e$ half-width in pixels that ranged from 0.3 to 0.5 pixels. The full set of fittable parameters for a single image is thus, Pluto: x , y , flux, radius; Charon: x , y , flux, and image jitter and background level. All parameters could be solved for simultaneously, but this did not work well. Instead, the usual practice was to fit Pluto radius, jitter, and background with individual single-parameter optimizations. The rest of the parameters were then fitted together. As it was later determined, the inferred jitter amount is much too large to be due to the pointing control system on *HST*. In fact, the true jitter is not measurable in our data, but the fits to the data were definitely better when including this component. We accept it as a correction to the pixel-response function (PRF) that is built in to TinyTim. However, we did not try to get an ultra-precise determination and instead left it at reasonable levels after its initial fitting. The Pluto radius (top-hat filter size) turned out to be too correlated with the jitter term, so fits for this value were never used. Instead, we used a value of 0.97 pixels that is equal to the mean of the size of Pluto from all images. Small variations in the changing geocentric distance did not make enough difference to be worth varying this parameter.

The region of the image used for fitting was an 83 pixel square box centered on the original centroided location of Charon. Getting a well-behaved χ^2 value requires fixing the fitting region for the entire process. Prior to fitting, a centroid position was computed for Charon and should be within a pixel or two of the

Table 2
Cycle 15 WFPC2/PC Pluto and Charon Raw Positions

ID	JDT	Filter	Exp	Pl x	Pl y	Ch x	Ch y	Sky	Jit	χ_v^2
u9qa0101m	2454183.5195139	F555W	100	393.816(3)	434.630(6)	406.172(6)	436.891(6)	0.307	0.46	2.60
u9qa0102m	2454183.5215972	F555W	100	393.855(2)	434.616(6)	406.218(6)	436.926(6)	0.361	0.45	2.64
u9qa0103m	2454183.5231829	F555W	14	393.955(3)	434.699(3)	406.268(4)	437.027(12)	0.043	0.38	0.60
u9qa0104m	2454183.5245718	F555W	14	393.960(3)	434.741(3)	406.256(12)	437.104(12)	0.062	0.38	0.60
u9qa0105m	2454183.5285417	F555W	100	427.194(6)	468.488(6)	439.517(6)	470.918(4)	0.376	0.45	4.21
u9qa0106m	2454183.5306250	F555W	100	427.190(6)	468.471(6)	439.514(6)	470.943(4)	0.368	0.45	4.44
u9qa0107m	2454183.5327083	F555W	100	427.164(6)	468.432(6)	439.494(6)	470.959(4)	0.387	0.46	4.25
u9qa0108m	2454183.5347917	F555W	100	427.135(6)	468.429(6)	439.460(6)	470.993(12)	0.408	0.47	4.34
u9qa0109m	2454183.5368750	F555W	100	427.137(6)	468.437(6)	439.454(4)	471.032(12)	0.404	0.47	4.87
u9qa010am	2454183.5405440	F555W	14	360.243(6)	401.314(6)	372.496(12)	403.960(12)	0.059	0.44	0.84
u9qa010bm	2454183.5419329	F555W	14	360.241(6)	401.302(6)	372.456(12)	403.991(12)	0.089	0.45	1.14
u9qa010cm	2454183.5438194	F555W	100	360.096(6)	401.256(6)	372.403(12)	403.986(12)	0.434	0.49	5.42
u9qa010dm	2454183.5459028	F555W	100	360.093(6)	401.248(6)	372.388(12)	403.997(12)	0.406	0.49	5.67

Notes. All positions are in raw chip 0-indexed pixel coordinates. Time units are in days, and all positions and uncertainties are in pixels. Uncertainties are given in parentheses for the last digits of the position. Sky is in units of DN, exposure times are in seconds, jitter is in pixels, and χ^2 is per degree of freedom.

(This table is available in its entirety in FITS format in the online journal. A portion is shown here for guidance regarding its form and content.)

correct answer. The Pluto field was somewhat crowded in 2007, and field stars were often present in the images in locations that impinged on the fitting box. The field stars were independently fitted in the long-exposure data and then subtracted prior to the fitting process.

During the fitting process, we used a pixel mask that recorded non-fittable pixels, usually energetic particle events (aka cosmic-ray strikes) and saturated pixels. Any pixels flagged were excluded from the computation of χ^2 and thus did not influence the fit. The masks were generated by a combination of automatic routines and final visual inspection of all flagged pixels. The visual inspection was able to correct for algorithm errors that either flagged good pixels bad or let through bad pixels. After the image was prepped by removing stars and flagging bad pixels, it was then given to the fitting program. This fitting process had to be iterated with the star fitting step until both converged. The final fitted positions are in the distorted optical system of WFPC2/PC and were corrected using the coefficients determined by Anderson & King (2003).

The fits are weighted by the original uncertainty of each pixel before any sources are subtracted. The uncertainties are photon noise summed in quadrature with the read noise of the detector. The per-pixel noise is set to 1.5 DN if the computed value is less. The final results of this fitting process are provided in Table 2. Due to the length of the data set, the printed table just shows the structure of the electronically available file that contains all observations. The goodness of fit tabulated is χ_v^2 , which is the weighted χ^2 divided by the number of constraints minus the number of free parameters. In general, the longer exposures have a larger χ_v^2 than the shorter, non-saturated, exposures. The uncertainties in this table are computed by finding the position in the positive and negative direction from the best fit where the χ^2 value increased by one. The larger of the two is kept as the 1σ error for that coordinate. The final distortion-corrected sky-plane offsets of Charon from Pluto are included in Table 4. The uncertainties in this final table come from adding the per-axis error together in quadrature and taking that as the final error in both sky-plane coordinates.

4.4. HST Cycle 17: WFC3, 2010

These observations were hoped to be once again with the ACS/HRC camera if it could be repaired during the servicing

mission. Unfortunately, that repair was unsuccessful despite the best efforts of engineers and astronauts alike. The loss of HRC means we cannot get additional spatially resolved data on Pluto at visible wavelengths other than what we expect to get from the New Horizons encounter in 2015. This sparse sampling makes it very challenging to understand the dynamic changes taking place on Pluto at its current seasonal epoch.

The observations were re-designed to use the new camera, WFC3. The new camera is a big improvement over the WFPC2 camera in having lower readout noise, faster and more flexible readout, and overall much lower operational overhead. Its spatial resolution is no match for the lost ACS/HRC camera but still permits high-quality astrometric measurements.

The WFC3 camera shares one difficult attribute with ACS, and that is a strong optical field distortion. Despite this similarity, we chose to implement a much simpler fitting process than that used for ACS. As before, the PSF library is maintained as a set of PSF images on a 50 pixel grid spacing. However, the PSFs are distorted by the TinyTim software, and we use these distorted PSFs to build our model images rather than build model images that are distorted by TinyTim. As a result, these distorted PSFs are not interpolatable and can only be used as convolution kernels. Thus, the sub-pixel position of the object must be carried in another way. For this implementation we again use the top-hat representation for the objects but require a minimum 0.5 pixel radius size for any object (including stars and very small satellites). Any size smaller than this would lead to positional discretization in the model images and confuse the minimization routines. Pluto is set to 1.25 pixel radius and Charon to 0.625 pixel radius for this camera due to the slightly finer pixel scale than provided by WFPC2/PC. The jitter term in our software was left disabled. The PSFs were computed with both versions 7.1 and 7.4 of TinyTim, though the version 7.1 tool had non-trivial modifications based on pre-release updates being made to TinyTim following the commissioning of WFC3. The fit quality is actually better with our version 7.1 calculations, but given the difficulty in documenting the changes, we are presenting only version 7.4 based results in this work. It is possible that our minimum-size top hat was serving partially like a PRF and compensating for a deficiency in version 7.1. Now, in 7.4 we find that the PSFs tend to be slightly too wide in the central core. We could improve the shape by removing our top hat, but doing so would critically damage our ability

Table 3
Cycle 17 WFP3/UVIS1 Pluto and Charon Raw Positions

ID	Object	JDT	Filter	Exp	dw	x	σ_x	y	σ_y	Sky	σ_{sky}	χ^2_{ν}
ib4w01i5q	Charon	2455310.81137	F350LP	3	15	269.757	0.025	261.692	0.025	0.731	0.006	4.49
ib4w01i5q	Pluto	2455310.81137	F350LP	3	15	255.019	0.012	257.814	0.004	0.731	0.006	4.49
ib4w01i6q	Charon	2455310.81241	F350LP	3	15	272.355	0.025	264.238	0.025	0.696	0.006	4.21
ib4w01i6q	Pluto	2455310.81241	F350LP	3	15	257.590	0.006	260.294	0.004	0.696	0.006	4.21
ib4w01i7q	Charon	2455310.81357	F350LP	23	15	271.321	0.012	261.676	0.012	5.276	0.008	10.05
ib4w01i7q	Pluto	2455310.81357	F350LP	23	15	256.587	0.006	257.686	0.012	5.276	0.008	10.05
ib4w01i8q	Charon	2455310.81484	F350LP	23	15	273.786	0.012	264.285	0.012	5.292	0.008	9.92
ib4w01i8q	Pluto	2455310.81484	F350LP	23	15	259.067	0.012	260.315	0.012	5.292	0.008	9.92
ib4w01i9q	Charon	2455310.81712	F350LP	197	25	274.222	0.025	261.501	0.025	43.269	0.018	26.35
ib4w01i9q	Pluto	2455310.81712	F350LP	197	37	259.635	0.025	257.686	0.051	43.269	0.018	26.35
ib4w01iaq	Charon	2455310.82041	F350LP	197	25	276.781	0.025	264.075	0.025	43.304	0.019	25.55
ib4w01iaq	Pluto	2455310.82041	F350LP	197	37	262.171	0.025	260.125	0.025	43.304	0.019	25.55
ib4w01ibq	Charon	2455310.82293	F438W	12	15	272.683	0.051	262.478	0.051	0.192	0.006	5.20
ib4w01ibq	Pluto	2455310.82293	F438W	12	15	258.032	0.025	258.346	0.007	0.192	0.006	5.20
ib4w01icq	Charon	2455310.82407	F438W	12	15	275.215	0.051	264.927	0.051	0.230	0.006	5.24
ib4w01icq	Pluto	2455310.82407	F438W	12	15	260.500	0.007	260.713	0.025	0.230	0.006	5.24
ib4w01idq	Charon	2455310.82522	F438W	12	15	272.832	0.051	263.649	0.051	0.002	0.006	5.41
ib4w01idq	Pluto	2455310.82522	F438W	12	15	258.184	0.025	259.454	0.007	0.002	0.006	5.41
ib4w01ieq	Charon	2455310.82637	F438W	12	15	275.355	0.051	266.256	0.051	0.121	0.006	5.28
ib4w01ieq	Pluto	2455310.82637	F438W	12	15	260.656	0.007	261.974	0.025	0.121	0.006	5.28

Notes. All positions are in raw chip 0-indexed pixel coordinates. Time units are in days, and all positions and uncertainties are in pixels. Sky is in units of DN, exposure time is in seconds, and χ^2 is per degree of freedom.

(This table is available in its entirety in FITS format in the online journal. A portion is shown here for guidance regarding its form and content.)

to measure positions. We could perhaps eliminate this problem with an ad hoc adjustment of the PRF to compensate for the top-hat approximation, but this effort was beyond the scope of this work. The effect on the Pluto and Charon fitting seems to be minimal, though. The largest error comes when working on the faint satellites, but this problem will be discussed in a separate report.

The data were taken with the F350LP, F438W, and F555W filters with short-, medium-, and long-exposure times just as for the Cycle 15 data. However, only the F350LP data include the longest exposures, where the signal-to-noise ratio on the faint satellites was a driving issue. Again, the medium- and long-exposure data saturate Pluto and Charon, even more than for the Cycle 15 data.

As with the Cycle 15 fit, we use photon-noise-based weighting and a noise floor of 1.3 DN. Flagging bad pixels is done entirely by hand and only near the fitting region. Rather than fit stars, we just blotted them out as we do for energetic particle events. The sky background was never fitted in these data and simply measured from the image with a robust sky level estimation tool. These data required a different handling of the fitting region from Cycle 15. For each exposure time a box half-width was chosen to include the fittable region for each object. For the short and medium exposures the half-width was set to 15 pixels for both Pluto and Charon. For the long F350LP exposures the half-width was set to 25 pixels for Charon and 37 pixels for Pluto. The larger size let us fit more pixels in the wings of the overexposed PSF. The final fitting region for the simultaneous fit to Pluto and Charon is a rectangle that just includes the relevant boxes for Pluto and Charon based on an initial centroid position. The position of the fitting region is fixed throughout all fitting.

In the bad pixel mask we started with a traditional cut for saturation to mark overexposed pixels. During the fitting process it became clear that non-saturated pixels near saturated (bleeding) pixels are systematically too bright. In response to

this we reduced the saturation limit by nearly a factor of two but still saw boundary effects around the flagged pixels. These boundaries were not in all directions, however, and exhibited systematic patterns such as immediately below and above the bleed trail, or just to the upper right of the source. The latter feature may well be an internal reflection or ghost image rather than a saturated pixel, but it was flagged just the same. Manual flagging was used to mark these extra pixels to be avoided.

The conversion of the raw-pixel positions to differential astrometry was done using the distortion correction information provided by STScI's Calibration Database System that is contained with the image headers of the FLT image data (Kozhurina-Platais et al. 2009). This information is compatible with the IDL Astronomy User's Library tool, `xy2ad`, that converts input CCD positions to absolute coordinates on the sky (right ascension and declination). The final differential astrometric positions are thus the offset to each satellite from Pluto. These relative measurements eliminate any astrometric zero-point error for the guide-star-based solution while leaving the differential distortion correction.

The computation of the errors was done just as it was for the Cycle 15 data, a value that is 1σ away from the best fit in χ^2 space. The raw fitted values are provided in Table 3. Due to the length of the data set, the printed table just shows the structure of the electronically available file that contains all the observations. The goodness of fit tabulated is per degree of freedom and tracks the number of pixels masked out. In general, the longer exposures have a larger χ^2 than the shorter, non-saturated exposures.

4.5. Fit Results

The orbit fitting tools used are nearly the same as used in the previous section for the synthetic astrometry. One subtle difference between the two fitting schemes is that the reported orbital elements come from the fit to the data rather than from an average of many trial fits. To compute the uncertainties on the

Table 4
Charon Astrometry

Instrument	Filter	Cycle	JDT	$\Delta\alpha$	$\Delta\delta$	σ	$\Delta\alpha_F$	$\Delta\delta_F$	σ_F
WFPC/PC	F555W	2	2448763.5719036	0.0201	0.7137	0.0024	0.0157	0.7169	0.0024
WFPC/PC	F555W	2	2448763.5760703	0.0206	0.7092	0.0024	0.0162	0.7124	0.0024
WFPC/PC	F555W	2	2448763.8399592	0.0643	0.5312	0.0024	0.0605	0.5335	0.0024
ACS/HRC	F555W	11	2452436.8217600	0.4455	0.1442	0.0020	0.4386	0.1427	0.0020
ACS/HRC	F555W	11	2452436.8229400	0.4457	0.1394	0.0020	0.4388	0.1379	0.0020
ACS/HRC	F555W	11	2452436.8241200	0.4483	0.1413	0.0020	0.4413	0.1398	0.0020
WFPC2/PC	F555W	15	2454183.5195139	-0.4956	-0.2860	0.0009	-0.4901	-0.2850	0.0009
WFPC2/PC	F555W	15	2454183.5215972	-0.4973	-0.2845	0.0009	-0.4918	-0.2836	0.0009
WFPC2/PC	F555W	15	2454183.5231829	-0.4961	-0.2824	0.0016	-0.4906	-0.2815	0.0016
WFC3/UVIS1	F555W	17	2455310.8113704	0.5251	0.3260	0.0010	0.5226	0.3239	0.0027
WFC3/UVIS1	F555W	17	2455310.8124097	0.5279	0.3251	0.0010	0.5254	0.3230	0.0027
WFC3/UVIS1	F555W	17	2455310.8135694	0.5284	0.3230	0.0005	0.5259	0.3210	0.0013

Notes. All positions are with respect to Pluto in J2000 coordinates. Time units are in days, and all positions and uncertainties are in arcsec. Offsets are tangent plane distances and include the $\cos \delta$ correction.

(This table is available in its entirety in FITS format in the online journal. A portion is shown here for guidance regarding its form and content.)

elements, we refit the data 40 times, each time adding Gaussian noise to each point according to its uncertainty. The standard deviation of each orbital elements from these 40 trials is then used as the uncertainty for the elements.

The data fitted are the final distortion-corrected sky-plane offsets of Charon from Pluto contained in Table 4. The complete data set is provided as an electronic supplement and includes a total of 899 measurements. The values shown in print provide examples of the content of the full file. For each measurement we provide the name of the camera and mode along with the filter used for that image. Also shown is the observing cycle on *HST*. This information is followed by the mid-time of the exposure. The positions ($\Delta\alpha$, $\Delta\delta$) followed by their uncertainties (measured or estimated) provide the J2000 offset in right ascension (α) and declination (δ) in arcseconds. These values represent the original measurements with no corrections applied. The uncertainties came from adding the per-axis error together in quadrature and taking that as the final error in both sky-plane coordinates. The last three columns list positions ($\Delta\alpha_F$, $\Delta\delta_F$) and uncertainties that have had corrections applied to remove systematic errors and scale the error bars. These corrections are the subject of a rather lengthy discussion later in this subsection.

A summary of different fits to the Charon astrometric data is provided in Table 5. We show previously published orbital elements in the top portion of the table along with references. The middle section from “Cycle 2_L ” down to “All” is the result of fitting the as-measured data. The subscript on the cycle is meant to remind the reader that some observations are COL (shortened to L) data while the Cycle 11 data are COB (shortened to B). The additional entry for “Cycle 11_L ” is a test data set that comes from adding the Buie et al. (2010b) map COL offset to the as-measured data to create a simulated data set that should have similar difficulties as any other COL data. The fit labeled “All” comes from fitting the original measured data exactly as tabulated in Table 4, meaning that it is a mix of both COL and COB data. For each data set there are two fits shown, one that is unconstrained and fits all Keplerian elements while the other is forced to be a circular orbit. The notation [0.] for the eccentricity is used to denote these constrained fits. For a constrained fit the value of $\tilde{\omega}$ is undefined and is not listed.

The residuals from the two-body fits show interesting patterns when plotted. There are too many such plots to include here, but a few key examples will suffice. Consider the residuals shown in Figure 7 from an unconstrained fit to the Cycle 11 data. There are

obvious patterns to the residuals that are maintained for many adjacent sets of observations. Each clump of data corresponds to a single orbit with *HST*, and these are essentially identical but independent measurements at the same geometry. As described in Buie et al. (2010a), this plot is not in time order, and in general adjacent clumps are likely to be nearly 6 months apart in time. That the structure is coherent when viewed against sub-Earth longitude on Pluto is strongly suggestive of the structure being related to albedo patterns on the surface of Pluto. If the map from Buie et al. (2010b) were perfect, the residuals in Figure 7 should not exhibit any patterns at all. Thus, this figure clearly shows that some residual astrometric difficulties remain with data that are otherwise supposed to be COB measurements.

The residuals shown in Figure 8 are for the same data as in Figure 7 except that the fit in this case was constrained to be perfectly circular. The most striking aspect of this figure is the *systematic* offset in the right ascension residuals. We did some tests on our fake data set to replicate this process to see if we could suppress a true eccentricity signature by subtracting a mean offset. In those tests the resulting orbit fits were slightly noisier, but none of the elements were affected, including eccentricity. There is also a smaller but no less important systematic offset in declination. These shifts are a fundamentally important clue that we will come back to shortly. Aside from the systematic errors, we also see similar coherent patterns between the two residual plots that correlate from one clump to the next. These coherent patterns are common to *all* plots for every data set and orbit fit we attempted.

The situation shown in Figure 9 is even worse. Here we have taken the map that was derived from the Cycle 11 data and compute the COL offset. This COL offset is then added to the notional COB measurements to give us astrometry that is COL based. This is exactly the type of data we have in all other data sets and serves as a useful reference. We show here the residuals from a constrained circular fit. The systematic shift and modulations are even stronger here and according to χ^2 are a much worse fit than the COB data, as expected. Clearly, the albedo map has done much good in cleaning up the astrometric data.

For a final comparison we show the residuals from a constrained circular fit to the Cycle 17 data set, seen in Figure 10. Again, we see systematic shifts and modulations. The modulations are more or less coherent from one data set to the next. If you look carefully, you will see that the placement of highs

Table 5
Two-body Orbit Fits to Charon Astrometry

Data Set	P (days)	a (km)	e	i (deg)	L (rad)	Ω (rad)	$\tilde{\omega}$ (rad)	$ \overline{O - C} _{\alpha}$ (mas)	$ \overline{O - C} _{\delta}$ (mas)	χ^2_{ν}
T85	6.387640	19360	[0.]	94.079	...	3.84716	...			
TBS87a	6.387204	19130	[0.]	91.789	...	3.89270	...			
TBS87b	6.387217	19130	[0.]	98.289	...	3.89126	...			
TB88	6.387200	19640	[0.]	98.489	...	3.89174	...			
BGT89	6.387219	19640	[0.]	98.489	...	3.89139	...			
TB97	6.387223(17)	19636(8)	0.0076(5)	96.163(32)	4.5022(8)	3.8920(4)	3.824(38)			
B06	6.387230(1)	19571(4)	0.00000(70)	96.145(14)	4.5020(2)	3.8929(2)	...			
T08	6.38720	19570	0.0035	96.168	4.5023	3.8930	2.756			
Cycle 2 _L	6.387217(4)	19635(8)	0.0076(9)	96.167(24)	4.5065(24)	3.8921(6)	3.825(30)	1.9	2.4	0.99
	6.387219(10)	19616(8)	[0.]	96.160(27)	4.5054(56)	3.8910(6)	...	2.1	3.0	1.86
Cycle 11 _B	6.387269(6)	19563(3)	0.00434(13)	96.139(14)	4.50259(26)	3.89342(22)	0.348(17)	1.4	1.8	1.08
	6.387290(6)	19562(3)	[0.]	96.131(11)	4.50264(27)	3.89345(22)	...	1.3	1.3	2.54
Cycle 11 _L	6.387288(5)	19574(4)	0.00899(13)	95.971(12)	4.50497(28)	3.89313(24)	3.548(8)	1.6	2.0	1.37
	6.387240(5)	19575(4)	[0.]	95.991(14)	4.50486(29)	3.89308(20)	...	1.9	2.6	7.56
Cycle 15 _L	6.387222(12)	19575(5)	0.00184(11)	96.068(19)	4.511(3)	3.89038(31)	6.07(6)	2.6	2.7	3.00
	6.387243(4)	19580(5)	[0.]	96.061(20)	4.5065(8)	3.89095(34)	...	2.3	2.4	3.54
Cycle 17 _L	6.387232(2)	19588(1)	0.00423(5)	96.223(8)	4.5052(7)	3.89186(16)	3.264(7)	1.9	1.6	7.99
	6.387232(1)	19590(2)	[0.]	96.198(9)	4.5042(3)	3.89317(15)	...	3.2	2.4	24.59
All	6.3872275(4)	19594(2)	0.00242(6)	96.198(9)	4.50423(27)	3.89317(15)	3.414(16)	3.2	2.4	6.52
	6.3872271(4)	19589(1)	[0.]	96.189(8)	4.50398(27)	3.89306(15)	...	3.3	2.3	7.96
Cycle 2 _F	6.387229(6)	19613(9)	0.0024(7)	96.284(33)	4.4966(33)	3.8920(6)	3.78(11)	2.1	2.2	0.93
	6.387220(21)	19605(11)	[0.]	96.282(30)	4.502(11)	3.8916(7)	...	2.1	2.2	1.00
Cycle 11 _F	6.387278(7)	19562(4)	0.00008(9)	96.133(12)	4.50258(25)	3.89343(25)	3.6(1.5)	1.3	1.3	0.64
	6.387278(6)	19562(3)	[0.]	96.133(15)	4.50258(26)	3.89343(19)	...	1.3	1.3	0.64
Cycle 15 _F	6.387271(10)	19570(5)	0.00020(12)	96.236(18)	4.5116(26)	3.89097(29)	4.8(1.0)	1.7	1.8	1.15
	6.387265(49)	19574(4)	[0.]	96.242(18)	4.510(12)	3.89121(29)	...	1.8	1.8	1.16
Cycle 17 _F	6.387257(7)	19588(5)	0.00007(10)	96.390(22)	4.5136(29)	3.89145(42)	5.8(2.0)	1.7	1.4	1.00
	6.387253(7)	19587(4)	[0.]	96.386(24)	4.5121(27)	3.89140(45)	...	1.7	1.3	1.00
2,11	6.3872229(8)	19569(3)	0.00006(9)	96.175(12)	4.50267(20)	3.89346(15)	1.6(1.3)	1.6	1.4	0.85
	6.3872224(11)	19568(3)	[0.]	96.171(10)	4.50254(28)	3.89331(22)	...	1.6	1.4	0.86
2,11,15	6.3872251(7)	19574(8)	0.00012(9)	96.189(12)	4.50198(39)	3.89284(32)	3.6(1.0)	1.7	1.6	1.00
	6.3872249(6)	19572(2)	[0.]	96.188(9)	4.50183(20)	3.89273(16)	...	1.7	1.6	1.00
2,11,15,17	6.3872274(7)	19573(6)	0.000030(75)	96.219(11)	4.50174(42)	3.89245(31)	4(1)	1.8	1.6	1.07
	6.3872273(3)	19573(2)	[0.]	96.218(8)	4.50177(18)	3.89249(12)	...	1.8	1.6	1.07

Notes. The Keplerian elements are given in J2000 coordinates at an epoch of JD = 2452600.5. The Cycle 17_F fit has its errors scaled up by $\times 2.652$.

References. T85: Tholen 1985; TBS87a: Tholen et al. 1987a; TBS87b: Tholen et al. 1987b; TB88: Tholen & Buie 1988; BGT89: Beletic et al. 1989; TB97: Tholen & Buie 1997; B06: Buie et al. 2006; T08: Tholen et al. 2008.

and lows in the residual pattern is similar to the Cycle 11 data. This coherency is to be expected if caused by albedo features. There will be some changes to the pattern, typically in amplitude, between data sets since the viewing geometry is somewhat different for each.

After looking at a few of these types of plots, one quickly gets overloaded with all the details of the patterns. To provide an overview, we extracted some key values from each of these types of plots. The dashed (green) line in these figures is the result of a LOWESS smoothed curve with a smoothing half-width of 90° . The data in the plots are replicated for one period before and one period after what is shown so that the smoothed curve will reflect a periodic function. The smoothed curve is evaluated (and displayed) at 1° intervals from 0° to 360° . The smoothing was done using weighting of $1/\sigma^2$, where σ is the uncertainty for each data point. From the smoothed curve we record the difference between the maximum and the minimum. This is the peak-to-peak amplitude of the coherent modulation in the residuals, denoted by $A_{\Delta\alpha}$ and $A_{\Delta\delta}$. We also record the mean of the points in the smoothed curve, denoted by $\overline{\Delta\alpha_s}$ and $\overline{\Delta\delta_s}$. These values are shown in Table 6 for all of the primary

Table 6
Summary Two-body Orbit Fit Residuals from Real Astrometry

Cycle	Dtype	Ftype	$\overline{\Delta\alpha_s}$ (mas)	$A_{\Delta\alpha}$ (mas)	$\overline{\Delta\delta_s}$ (mas)	$A_{\Delta\delta}$ (mas)
2	COL	u	0.008	2.7	0.165	4.5
2	COL	c	1.950	4.4	0.159	8.9
11	COB	u	-0.791	1.8	-0.287	4.9
11	COB	c	-3.572	1.7	-1.513	1.8
11	COL	u	0.595	4.6	-0.406	5.5
11	COL	c	6.576	4.7	1.452	7.4
15	COL	u	-0.743	6.7	-1.087	7.0
15	COL	c	-1.626	5.6	-2.799	5.1
17	COL	u	0.221	3.2	-0.212	2.2
17	COL	c	3.530	3.6	1.868	3.9
all	COB	u	-0.492	2.7	-0.198	2.2
all	COB	c	1.433	4.0	0.615	2.8
all	COL	u	0.191	3.1	-0.258	2.7
all	COL	c	3.370	4.1	1.237	4.4

Notes. u denotes an unconstrained two-body fit; c denotes a constrained circular fit.

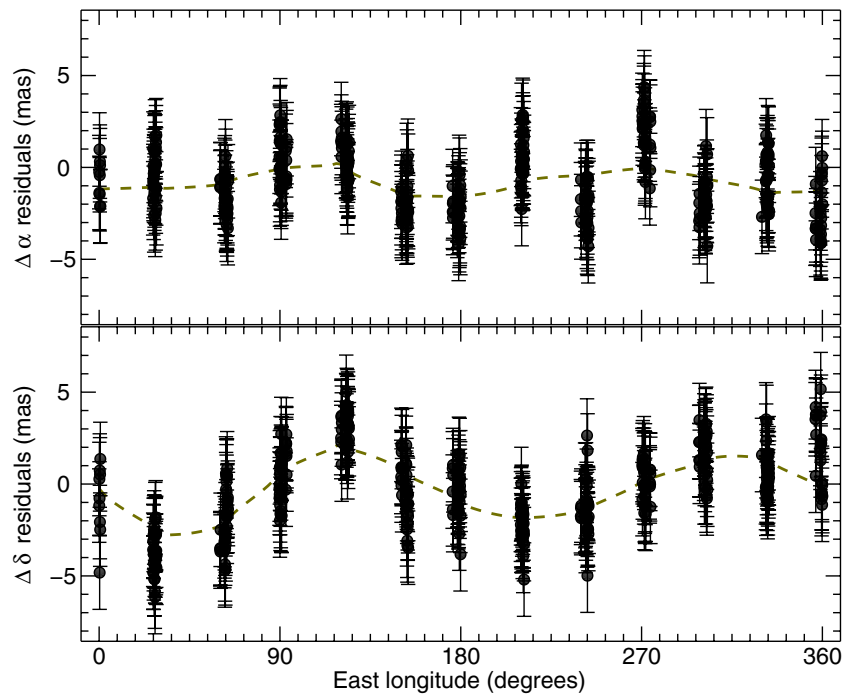


Figure 7. Post-fit residuals from Cycle 11 COB data. The top panel shows the residuals in right ascension (corrected for $\cos \delta$) in units of mas. These values are plotted against the sub-Earth longitude on Pluto. The dashed (green) curve is a smoothed version of the data that shows the non-random trends in the residuals. The bottom panel is the same except for showing the declination residuals.

(A color version of this figure is available in the online journal.)

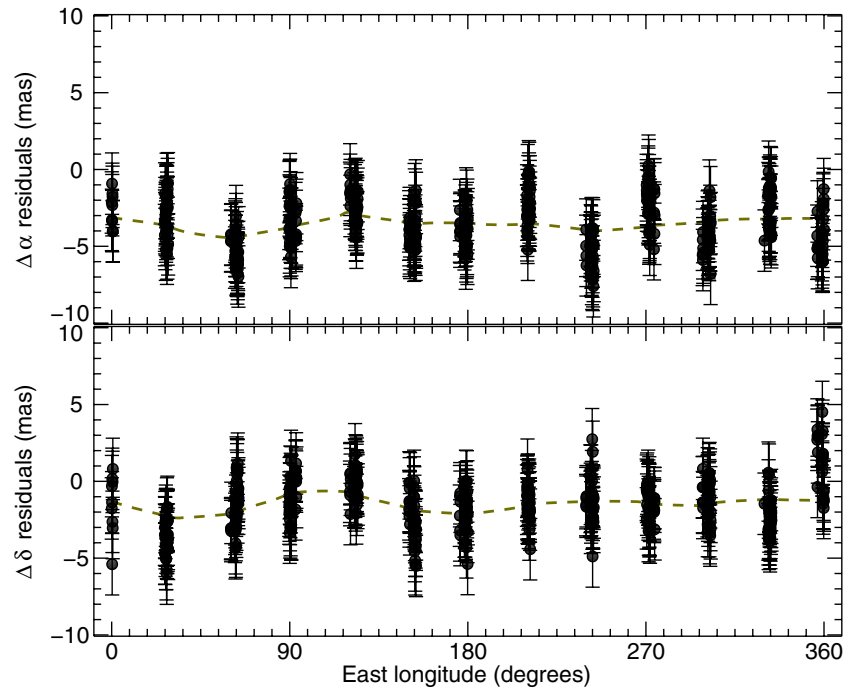


Figure 8. Post-fit residuals from constrained circular-orbit fit to Cycle 11 COB data. The top panel shows the residuals in right ascension (corrected for $\cos \delta$) in units of mas. These values are plotted against the sub-Earth longitude on Pluto. The dashed (green) curve is a smoothed version of the data that shows the non-random trends in the residuals. The bottom panel is the same except for showing the declination residuals.

(A color version of this figure is available in the online journal.)

data sets, as well as the Cycle 11 data with the COL offset added back into the data. Some of the smoothed curves show small but sharp deflections. This is a consequence of the non-uniform data sampling and, while cosmetically distracting, does not affect our results.

From the values shown in Table 6 there are a few important features that now become evident. Keep in mind that systematic patterns in right ascension residuals are dominated by latitudinal asymmetries in the map of Pluto. Note that the Cycle 11 COB data set has the lowest residual amplitude of all. The Cycle 11

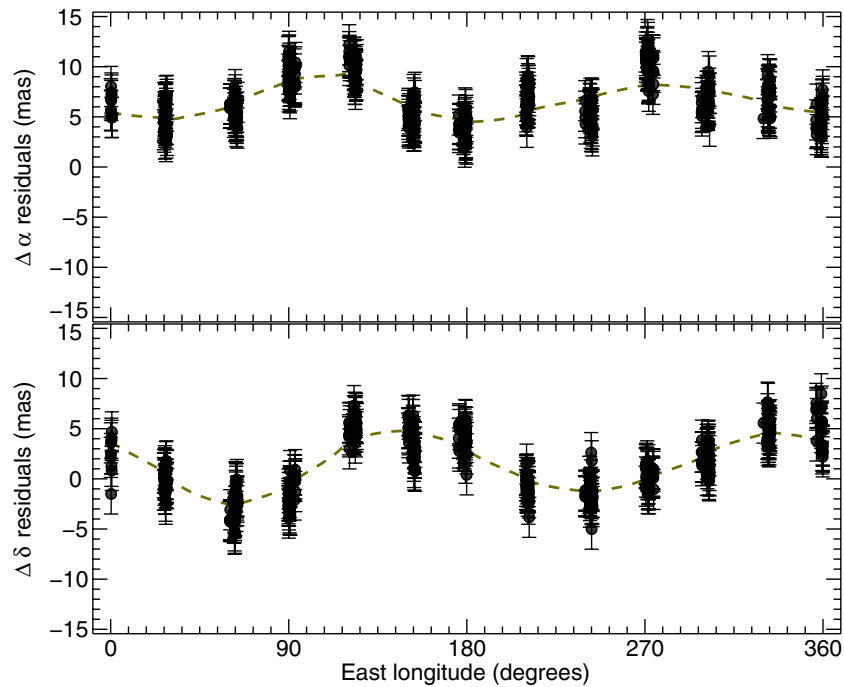


Figure 9. Post-fit residuals from constrained circular-orbit fit to Cycle 11 COL data. The top panel shows the residuals in right ascension (corrected for $\cos \delta$) in units of mas. These values are plotted against the sub-Earth longitude on Pluto. The dashed (green) curve is a smoothed version of the data that shows the non-random trends in the residuals. The bottom panel is the same except for showing the declination residuals.

(A color version of this figure is available in the online journal.)

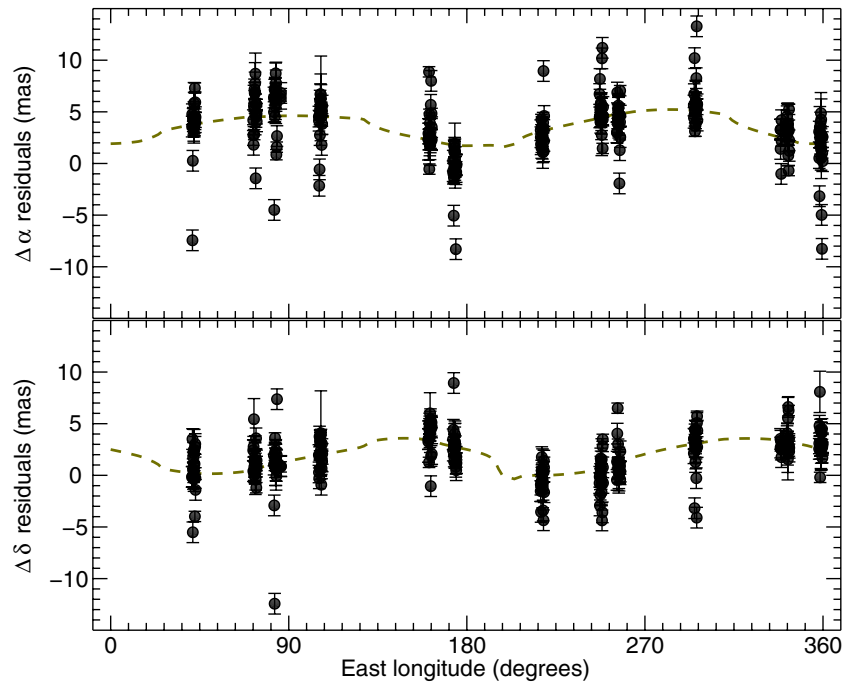


Figure 10. Post-fit residuals from constrained circular-orbit fit to Cycle 17 COL data. The top panel shows the residuals in right ascension (corrected for $\cos \delta$) in units of mas. These values are plotted against the sub-Earth longitude on Pluto. The dashed (green) curve is a smoothed version of the data that shows the non-random trends in the residuals. The bottom panel is the same except for showing the declination residuals.

(A color version of this figure is available in the online journal.)

COB circular fit also has one of the largest values of the residual mean. Guided by this realization, the Cycle 11 COB circular constrained fit has the highest ratio of mean residual to residual amplitude of all data sets and fits. This confluence of indicators is highly suggestive that there is something special about this data set.

The premise that will be pursued here is that the mean residual offset from the circular fit to the Cycle 11 COB data represents a systematic COL-COB error in the map. If true, failing to correct for this offset would corrupt the fitted orbital elements. Returning to the two-body fitting now, this corrected data set was fit with an unconstrained and a circular fit. These results are

Table 7
COL Map Correction Offsets

Cycle	ϕ (deg)	P.A. (deg)	Δ (AU)	Δ_{\parallel} (mas)	Δ_{\perp} (mas)	Δ_{α} (mas)	Δ_{δ} (mas)	$a\Delta_{\alpha}$ (mas)	$a\Delta_{\delta}$ (mas)
2	10.3	262.9	29.346	-3.476	2.428	-3.749	-1.980	-3.907	1.290
11	31.3	254.2	29.883	-3.025	2.428	-3.572	-1.513	-3.572	-1.513
15	40.4	246.6	30.598	-2.690	2.428	-3.434	-1.160	-4.413	-4.067
17	44.4	241.1	31.023	-2.524	2.428	-3.383	-0.906	0.903	-0.293

labeled as “Cycle 11_F” in Table 5. These two fits give essentially the same answer—the eccentricity is now easily consistent with zero. Note that the χ^2 value is below unity, indicating that our uncertainty estimation was too large in our past treatment of the Cycle 11 data. If we were to adjust the errors based on this fit, the adopted uncertainty would drop from 2 mas down to 1.6 mas. After the correction is applied, the residuals now appear to be much more reasonable, with a mean value of $(-0.070, 0.003)$ mas for the unconstrained fit and $(-0.017, 0.010)$ mas for the circular fit, while the amplitude of the residual pattern remains the same at 1.7 mas for both.

This result for the eccentricity implies that the orbit of Charon is circular to within 3 km. That there are still non-random variations in the residuals points to further inadequacies in the albedo map, but these largely appear to be adding only random noise to the fitting process—the mean offset of all visits is now zero though there are still systematic per-visit offsets. If the map were perfect, the per-visit offsets would also be zero and we would expect the orbit to be even better constrained. It has long been a concern to us that our astrometric errors appear to be so much larger for Pluto and Charon than what we routinely achieve on much fainter binary trans-Neptunian objects (Grundy et al. 2007). We seem to have taken a step for the better here though clearly the map corrections set the ultimate noise floor for this type of astrometry. Note that this has important implications for astrometry of Pluto and Charon with other filters. The Buie et al. (2010b) map is relevant for a single epoch (2002–2003) in *B* and *V* filters. Including other wavelengths (F350LP on *HST* or *JHK* on Keck, for example) still requires correction to any COL measurement albeit with less information from which to deduce a correction.

We then applied this methodology to the other data sets by correcting, as best as possible, for the COL–COB offset so that the measurements reflect a COB position for Pluto. Note that we are assuming COL = COB for Charon. The much smaller light-curve amplitude makes this a more reasonable assumption, and the smaller size of Charon further reduces the size of the effect. Without data of significantly higher spatial resolution this will remain a necessary approximation. The offset we applied to the Cycle 11 data is a vector offset on the plane of sky at the epoch of those data. The offsets used for each data set are summarized in Table 7. Most of the offset is in the direction parallel to the pole of Pluto’s rotation axis (still assumed to be parallel and coincident with the pole of Charon’s orbit). The component in the direction of the pole is likely to be projected in accordance with the mean sub-Earth latitude. Thus, at an epoch closer to the equator (e.g., Cycle 2) the parallel direction offset should be larger. Further from the equator (Cycle 15 and later), the offset should be smaller. We really do not know how to scale this since it depends on the latitudinal albedo distribution, but as a working approximation we chose to characterize the projection as a simple cosine function. Thus, the parallel offset can be represented as $\Delta_{\parallel} = \Delta \cos \phi$, where Δ_{\parallel} is the offset in the

parallel direction at some epoch, Δ is the full offset, and ϕ is the sub-Earth latitude at the epoch. The offset in the perpendicular direction is left unchanged. The offset measured for Cycle 11 can thus be converted to Δ_{\parallel} and Δ_{\perp} at $\phi = 31^{\circ}1$ and a pole position angle of P.A. = $254^{\circ}2$. To use these offsets, they must be re-projected onto the sky plane and are denoted as Δ_{α} and Δ_{δ} . As will become clear in a moment, these offsets were not enough to fully correct the data. The last pair of columns, labeled $a\Delta_{\alpha}$ and $a\Delta_{\delta}$, are the final adjusted offsets that give us the final corrected positions from Table 4.

The steps required to go from observed astrometry to corrected astrometry for data other than Cycle 11 using the values in Table 4 can be summarized as follows:

1. Correct COL data to COB using the offset computed from the Buie et al. (2010b) map based on the full geometry of each data point.
2. Add the projected Cycle 11 systematic error correction to the data (Δ_{α} , Δ_{δ}).
3. Compute mean plane-of-sky offsets from the residuals of the per-epoch fits to the data corrected with the steps this far. Add these offset to results of the previous step to get the final correction ($a\Delta_{\alpha}$, $a\Delta_{\delta}$).
4. Add the final correction to the map-corrected astrometry from step 1. This is the final-corrected astrometry.

As noted, these offsets are expected to be functions of both time and wavelength, but these functions are not currently characterizable with available information. It is useful to note that the Cycle 11 data are an equal combination of *B* and *V* data and they appear to both be corrected by the same offset. Since the maps do have color structure, this may be an indication of a systematic measurement error in just the Cycle 11 data since the method of extracting positions was quite different from the PSF fitting process used for the other data sets.

If the Cycle 11 based offsets were universally applicable to all data and our scaling methodology were perfect, the bias correction should have fixed all the data sets. This was not the case. Applying the scaled correction did make some improvement, but there were still clearly systematic biases in the residuals. Therefore, we computed a final bias correction from these partially corrected residuals and applied this last adjustment to all but the Cycle 11 data. The aggregate correction values are shown in the last two columns of Table 7. The need for an extra correction is clearly required by the data. The origin of the correction is less clear. Temporal variability in the map is one obvious factor that could lead to this extra correction, but our results only provide a suggestion, not proof, that this variation in shift is caused by changing albedo patterns.

We come now to the last group of fits shown in Table 5. These fits are all labeled with the “*F*” subscript and are the result of applying the final aggregate correction to the astrometry and fitting each cycle’s data independently. These independent fitting results now provide a consistent set of orbital elements

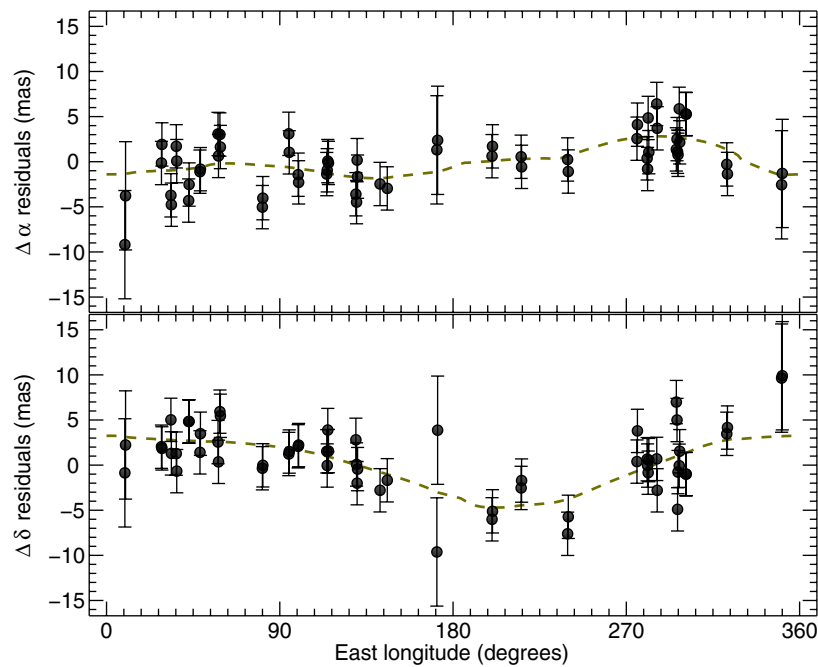


Figure 11. Cycle 2 residuals from the adopted circular two-body fit based on all data. The top panel shows the residuals in right ascension (corrected for $\cos \delta$) in units of mas. These values are plotted against the sub-Earth longitude on Pluto. The dashed (green) curve is a smoothed version of the data that shows the non-random trends in the residuals. The bottom panel is the same except for showing the declination residuals.

(A color version of this figure is available in the online journal.)

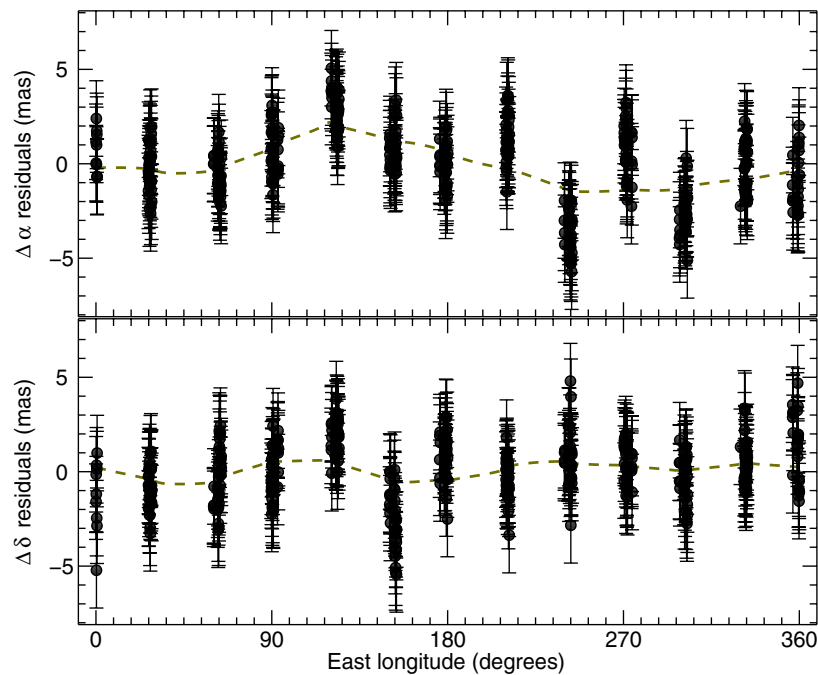


Figure 12. Cycle 11 residuals from the adopted circular two-body fit based on all data. The top panel shows the residuals in right ascension (corrected for $\cos \delta$) in units of mas. These values are plotted against the sub-Earth longitude on Pluto. The dashed (green) curve is a smoothed version of the data that shows the non-random trends in the residuals. The bottom panel is the same except for showing the declination residuals.

(A color version of this figure is available in the online journal.)

and all point uniformly to a very low eccentricity for Charon's orbit that is actually consistent with being zero. This consistency is encouraging and is taken as vindication of our application of this bias correction to the astrometry even if we do not know its exact source. The final three fits in Table 5 come from combining data sets to increase the time base of the observations. The final set of elements is from all our data. The choice to use the

restricted circular fit or the unrestricted fit does not matter as the elements are virtually the same for both. In our subsequent analysis, we have adopted the constrained circular fit as the final result of this work for the orbit determination. The post-fit residuals from our adopted fit can be seen for each data set in Figures 11–14. In the case of the Cycle 17 data, the final χ^2 values from the fits to the corrected and aggregate

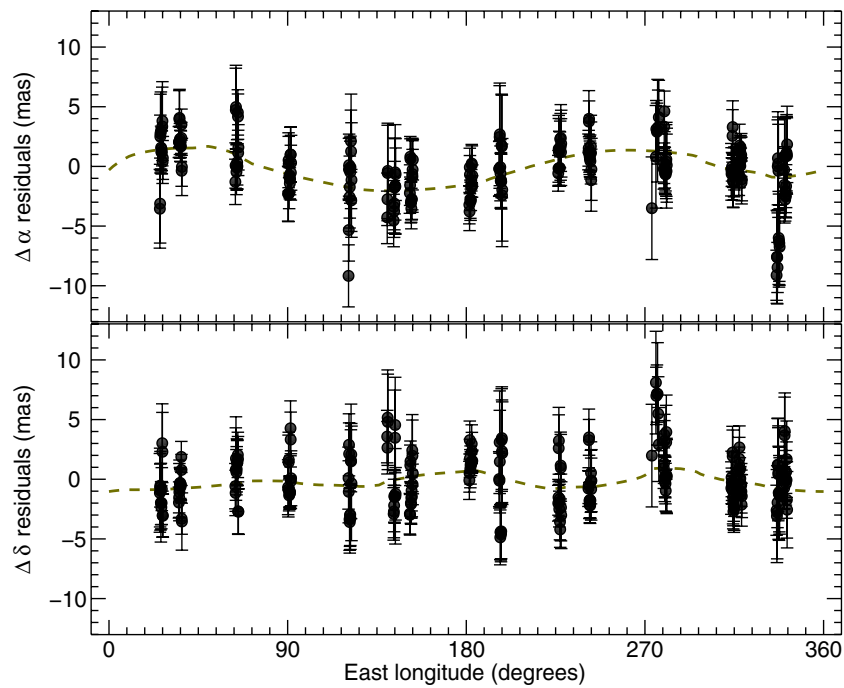


Figure 13. Cycle 15 residuals from the adopted circular two-body fit based on all data. The top panel shows the residuals in right ascension (corrected for $\cos \delta$) in units of mas. These values are plotted against the sub-Earth longitude on Pluto. The dashed (green) curve is a smoothed version of the data that shows the non-random trends in the residuals. The bottom panel is the same except for showing the declination residuals.

(A color version of this figure is available in the online journal.)

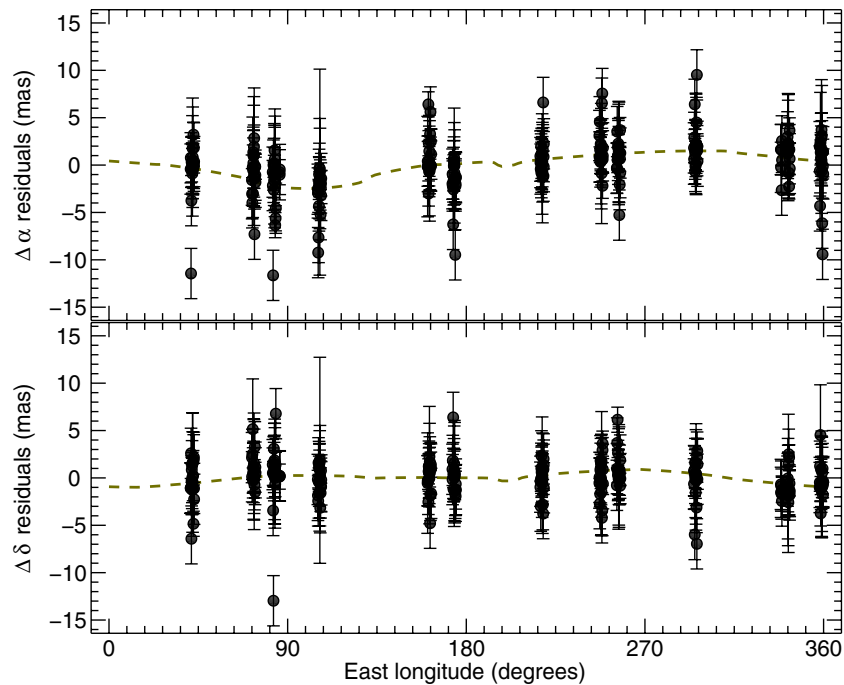


Figure 14. Cycle 17 residuals from the adopted circular two-body fit based on all data. The top panel shows the residuals in right ascension (corrected for $\cos \delta$) in units of mas. These values are plotted against the sub-Earth longitude on Pluto. The dashed (green) curve is a smoothed version of the data that shows the non-random trends in the residuals. The bottom panel is the same except for showing the declination residuals.

(A color version of this figure is available in the online journal.)

data were consistently too large. We attribute this to optimistic uncertainties and applied a uniform scaling factor of 2.652 to the measured uncertainties to bring χ^2_v for the individual fit down to unity.

The patterns in the residuals show non-random fluctuations that are coherent when viewed against the sub-Earth longitude

on Pluto. The Cycle 2 residuals shown in Figure 11 are centered on zero in each axis by virtue of the corrections that have been applied. The systematic deviations from zero are shown with the superimposed dashed line. These deviations are easiest to understand as residual errors on the COL-COB correction. This epoch is the furthest from the epoch of the map used for

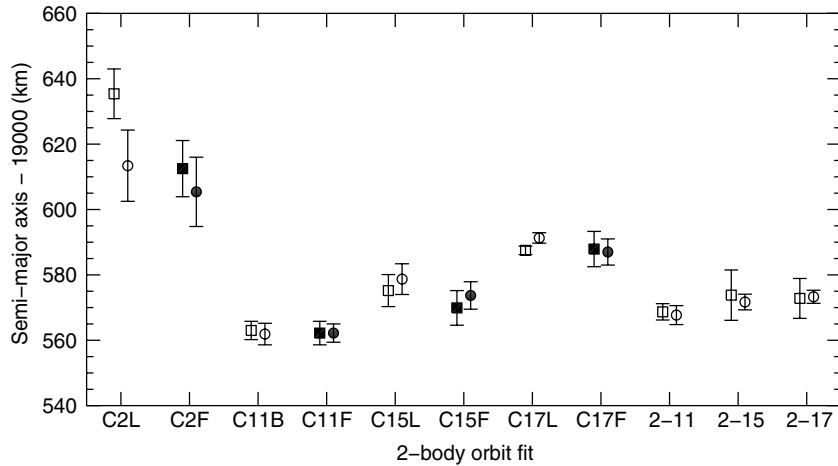


Figure 15. Graphical summary of semimajor axis from two-body fits. These values are taken from Table 5, where C# is shorthand for the cycle the data came from. In all cases, the final (F) solution is shown. For each cycle, the fit to the original astrometry (either COB shorted to B, or COL shortened to L). The last three are the final three aggregate fits. The squares show the unconstrained fit results, while the circles show the restricted circular fits. The filled symbols highlight the individual cycle fits after all corrections.

the corrections. These variations are providing information on changes in the surface albedo distribution. Further work will be required to invert this information into constraints on the maps themselves. In this case there is a large change between the longitudes of light-curve minimum (90°) and maximum (210°).

The residuals from the Cycle 11 data shown in Figure 12 show very little systematic trends in declination, but modulations are still evident in right ascension. Of all the data sets this one should be the best simply because the map is contemporaneous. Still, the variations seen here clearly show that the map still suffers from some as yet uncharacterized errors. The presence of these errors is not particularly surprising, but it does help to place constraints on the map errors. The worst errors at this epoch seem to be between minimum and maximum light.

Both the Cycle 15 residuals (Figure 13) and the Cycle 17 residuals (Figure 14) are very similar. Both data sets show almost no declination trend similar to Cycle 11. The right ascension trends are meaningful but do not correlate with key light-curve features. The amplitude in Cycle 15 is ± 2 mas, while the Cycle 17 data show a slightly larger amplitude at ± 3 mas. This change is probably not significant, but the shape and phasing of the residual patterns are different. Changes of this type indicate longitudinal albedo migration.

4.6. Image Scale

In our ongoing analyses we have become sensitized to apparently statistically meaningful signatures suggesting small systematic errors in the calibrated image scales of the different detectors used on *HST*. Based on the published calibrations for these instruments (MacKenty et al. 1992; McMaster & Biretta 2008; Maybhate et al. 2010; Dressel 2010), it is reasonable to assume internal consistency between ACS, WFPC2, and WFC3 (Cycles 11–17). WFPC (Cycle 2, pre-COSTAR) was not calibrated by the same methods or in the same level of detail and could be different. However, our own work (Tholen & Buie 1997) generated an accurate plate scale based on the heliocentric orbital motion of Pluto. We believe this method to be the most immune to small but meaningful systematic errors.

The results for semimajor axis from Table 5 are presented in Figure 15. The Cycle 2 results stand out from the rest of the determinations, with the biggest difference being between Cycle 2 and Cycle 11 prior to any corrections. The spread is less

in the corrected astrometry solutions (ending in F). In the case of C2F (unconstrained) and C11F (unconstrained) we find a 4σ discrepancy. However, this discrepancy is less compelling when we also consider the Cycle 15 and 17 data. Since the Cycle 11, 15, and 17 data all share a common calibration heritage, they must be treated as a set. The disagreement between these cycles may be showing us the true noise level in determining the semimajor axis. In the context of this larger noise level, the Cycle 2 results are no longer discrepant. Note that the formal error on the Cycle 2 image scale from Tholen & Buie (1997) translates to 2.6 km and is at a level generally smaller than the error on semimajor axis, certainly for a fit based on a single epoch of data. These results do not provide any compelling evidence for a scale error in the astrometry between *HST* cameras. In fact, the quality of the aggregate fits is quite good and does not show any unusual residuals by cycle that might corroborate an image scale problem. Breaking down χ^2_v by cycle on the final aggregate fit (“2, 11, 15, 17” from Table 5), we see $\chi^2_v = 1.49$ for Cycle 2, $\chi^2_v = 0.85$ for Cycle 11, $\chi^2_v = 1.23$ for Cycle 15, and $\chi^2_v = 1.16$ for Cycle 17 (with scaled errors).

The double occultation result from Sicardy et al. (2011) provides an interesting comparison with our fitting results. That work extracted a very precise position of Charon relative to Pluto of 0.5462 ± 0.0002 east and 0.2071 ± 0.0011 north at 2008 June 22 19:20:33.82 UT. The final “2–17” orbit solution predicts an offset of (0.5468, 0.2066) at that time. The difference is (−0.6, 0.5) mas and is quite close without being included in the fitting process. In the Sicardy analysis, the occultation measurements seemed to indicate a preference for the Cycle 2 semimajor axis (with our concurrence). However, in light of these new fits there is no longer any need to invoke a plate scale error to explain the occultation data.

5. DISCUSSION

The numerous possible combinations of data and adjustments for systematic errors, albedo effects, and incorrect uncertainties and their effects on the resulting fitted orbit are seemingly boundless. Regardless, there are some simple relationships that are useful to keep in mind. The uncertainty in the period is largely driven by the time base of the observations. As the simulations and actual data fitting show, increasing observational

baseline decreases the uncertainty on the period. Simple estimates can guide our expectation of how position error and time base relate to the accuracy with which we can determine the period. The *HST* data set now spans 20 years and is a testimony to the longevity and quality of this amazing facility. At the present time, the geocentric distance to Pluto implies an angular scaling factor of 4.4 mas = 100 km. To make the numbers round, consider the canonical uncertainty of an *HST* measurement to be 2.2 mas (or 50 km). The change in period that corresponds to this positional error is 23×10^{-7} days. This accuracy is what would result from two ideal measurements spaced 20 years apart. In reality, we do a least-squares fit to considerably more data than that, and we expect the positional error to be even smaller. The fits prior to the bias corrections are rarely consistent to within the measured or even the expected errors. After the correction, the fitted period is now consistent with the time base and data used. The final adopted solution from Table 5 has an uncertainty 10 times smaller than our simple estimate above. In fact, from a simple \sqrt{N} scaling of the uncertainty ($N = 899 * 2$) we might expect it to be another factor of four smaller still.

This ephemeris should be very useful in revisiting the mutual event data. Combining the actual shape of the event light curves as well as their timing constraints can still add to the knowledge of the orbit and the time history of the surface albedo. It still remains to harness the full value of the mutual event data by combining it with the extensive *HST* data set with proper treatment of the photometric effects with a suitable map for each body.

Of course, the process of fitting the orbit is much more complicated than this discussion would indicate. In particular, there is a strong coupling between a (or P) and e in any orbit fitting process. We have been trying for decades to pin down the precise value of Charon's orbital eccentricity. Compared to a circular orbit, an eccentric orbit exhibits a change in the radial distance δr between periape and apoapse that is equal to $2ae$. The final orbit with an unconstrained fit gives a 1σ upper limit to the eccentricity of 7.5×10^{-5} and indicates that the orbit is circular to better than 3 km.

Looking ahead, we can estimate the positional error between Pluto and Charon at the time of the New Horizons encounter in 2015 if our adopted orbit were used for targeting. The single-cycle orbit fits would predict the position to within 60–70 km (Cycle 15 is two times worse, Cycle 17 is two times better). Combining cycles drops the positional uncertainty to 6 km, well below a level that matters for targeting New Horizons. We compared our new adopted orbit positions against the JPL PLU017 orbit for Charon and find differences as a function of sub-Earth longitude on Pluto that range from 17 to 159 km. The largest positional error is at a sub-Earth longitude of 90° , which is near minimum light. These errors will be well worth correcting but are still not as significant as the errors caused by the uncertainty in the time of closest approach.

6. CONCLUSIONS

Astrometry of the Pluto system is especially difficult owing to the confusing effect of Pluto's surface albedo patterns. We have presented in this work an analysis that, for the first time, adequately removes this pattern to reveal the orbit of Charon as circular to better than 3 km. The observations we analyzed should have been able to place an even tighter limit on the eccentricity and return even more precise values for the other orbital elements, but there is a limit to how well we can correct

for the effects of albedo. This work was made possible by four key factors: (1) high-quality stable data from *HST*, (2) many distinct epochs of data, (3) well-sampled longitude coverage, and (4) having a map of Pluto relevant to the wavelength of observation. Losing any one of these advantages makes it exceedingly difficult, if not impossible, to recognize and remove the systematic errors that inevitably appear in the data. The hardest factor to support is having a map for the surface. So far, we have limited map data at visible wavelengths and no data at other wavelengths. Extending this into the IR, for example, allows the use of modern AO-based systems to reach superb spatial resolution. Such data will also require building maps unless the COB position can be directly retrieved. Since the IR is also a region affected by materials that have strong spectroscopic signatures, these maps will be a very strong function of color and passband. Making effective use of astrometry in this spectral region will be especially challenging. Perhaps other simpler spectral regions, such as the submillimeter, will make it easier to obtain high-precision astrometry once the full ALMA array becomes available. There is no doubt that variations of albedo as a function of time will also have a negative impact on any astrometric analysis. The per-epoch corrections we make must remove much of the effects of this temporal variation, but it is not clear for how long this will work without new map data. Fortunately, we have the upcoming New Horizons encounter with Pluto that will provide vastly superior albedo maps and even some astrometric data that will be known to be referenced to COB. For now, the orbit determination from our analysis is more than adequate to predict the location of Charon relative to Pluto with sufficient accuracy for the needs of the upcoming encounter.

This paper is based on observations with the NASA/ESA *Hubble Space Telescope* obtained at the Space Telescope Science Institute, which is operated by the Association of Universities for Research in Astronomy, Incorporated, under NASA contract NAS5-26555. Support for this work was provided by NASA through grant numbers HST-GO-10786, HST-AR-10940, and HST-GO-11556 from STScI. This project also was made possible, in part, by the software development efforts of Doug Loucks, Peter Collins, and Amara Graps.

Facility: HST (WFPC, WFPC2, ACS, WFC3)

REFERENCES

- Anderson, J., & King, I. R. 2003, *PASP*, **115**, 113
 Beletic, J. W., Goody, R. M., & Tholen, D. J. 1989, *Icarus*, **79**, 38
 Buie, M. W., Grundy, W. M., Young, E. F., Young, L. A., & Stern, S. A. 2006, *AJ*, **132**, 290
 Buie, M. W., Grundy, W. M., Young, E. F., Young, L. A., & Stern, S. A. 2010a, *AJ*, **139**, 1117
 Buie, M. W., Grundy, W. M., Young, E. F., Young, L. A., & Stern, S. A. 2010b, *AJ*, **139**, 1128
 Dressel, L. 2010, WFC3 Instrument Handbook, Version 3.0 (Baltimore, MD: STScI)
 Grundy, W. M., Stansberry, J. A., Noll, K. S., et al. 2007, *Icarus*, **191**, 286
 Kozhurina-Platais, V., Cox, C., Petro, L., Dulude, M., & Mack, J. 2009, Instrument Science Report (WFC3 2009-033; Baltimore, MD: STScI), 33
 Krist, J. 2004, <http://www.stsci.edu/software/tinytim/tinytim.html>
 Lee, M. H., & Peale, S. J. 2006, *Icarus*, **184**, 573
 MacKenty, J. W., et al. 1992, Wide Field—Planetary Camera Instrument Handbook, Version 3.0 (Baltimore, MD: STScI)
 Maybhate, A., et al. 2010, ACS Instrument Handbook, Version 9.0 (Baltimore, MD: STScI)
 McMaster, M., & Biretta, J. 2008, WFPC2 Instrument Handbook, Version 10.0 (Baltimore, MD: STScI)

Press, W. H., Teukolsky, S. A., Vetterling, W. T., & Flannery, B. P. 1992, Numerical Recipes in C: The Art of Scientific Computing (New York: Cambridge Univ. Press)

Sicardy, B., Bolt, G., Broughton, J., et al. 2011, [AJ](#), **141**, 67

Tholen, D. J. 1985, [AJ](#), **90**, 2353

Tholen, D. J., & Buie, M. W. 1988, [AJ](#), **96**, 1977

Tholen, D. J., & Buie, M. W. 1997, [Icarus](#), **125**, 245

Tholen, D. J., Buie, M. W., Grundy, W. M., & Elliot, G. T. 2008, [AJ](#), **135**, 777

Tholen, D. J., Buie, M. W., & Swift, C. E. 1987a, [AJ](#), **92**, 244

Tholen, D. J., Buie, M. W., & Swift, C. E. 1987b, [AJ](#), **94**, 1681